Simulation of instability and sound production in a turbulent channel flow with an acoustic liner

David Marx, Robin Sebastian, Véronique Fortuné

To cite this version:

David Marx, Robin Sebastian, Véronique Fortuné. Simulation of instability and sound production in a turbulent channel flow with an acoustic liner. Journal of Sound and Vibration, 2024, 573, pp.118223. 10.1016/j.jsv.2023.118223 . hal-04528893

HAL Id: hal-04528893

https://hal.science/hal-04528893v1

Submitted on 2 Apr 2024

Simulation of instability and sound production in a spatial turbulent channel flow with an acoustic liner

David Marx[1], Robin Sebastian, Véronique Fortuné

Institut P', CNRS - Université de Poitiers - ENSMA
Site ENSIP, Bât B17, 6 rue Marcel Doré 86022 Poitiers CEDEX, France

Preprint accepted in: Journal of Sound and Vibration, 2023.
doi: https://doi.org/10.1016/j.jsv.2023.118223

Abstract Acoustic liners are used to absorb sound waves in ducts with flow. These liners can become unstable and some experiments have shown that in this case they do not damp sound as they should. This situation is addressed numerically. A turbulent plane channel flow at a friction Reynolds number of about 400 is computed using direct numerical simulation of the compressible Navier-Stokes equations. The channel is in spatial development, and the inflow is fully turbulent, non-reflecting, and can inject an incident acoustic wave. The liner is modeled by an acoustic impedance placed on a portion of the channel bottom wall. Several liners are simulated, stable or unstable. Spatial instabilities are observed and well modeled by a linear spatial stability analysis. The scattering of the instability at the liner trailing edge triggers backpropagating acoustic waves, as well as sound emission downstream of the liner. Backpropagating waves make a feedback loop possible on the liner, so that instabilities are observed even in convectively unstable situations without excitation. The effect of an incident acoustic wave is discussed.

Keywords: direct numerical simulation; turbulent channel flow; duct aeroacoustics; acoustic impedance

1 Introduction

Acoustic liners are used to absorb sound waves in ducts with flow, such as in aircraft aeroengines [1, 2, 3, 4]. Occasionally, these liners can lead to flow instability [5, 6, 7, 8, 9, 10, 11, 12, 13, 14, 15, 16]. This typically occurs when the liners have a small resistance [16] and a thin boundary layer [9, 10, 12], since this promotes momentum exchange between the material and the flow. Instabilities have been observed over single-degree-of-freedom liners [5, 8] and over porous surfaces [17]. A manifestation of instability is the existence of a surface wave [18, 19] along the wall, which is mainly vortical and can be described by incompressible equations [13]. Another effect is abnormal sound amplification [5, 6, 8, 14] by the liner, meaning some energy of the flow is transferred to sound waves. This amplification occurs close to the resonance frequency of the liner,

---

[1] Corresponding author david.marx@univ-poitiers.fr

that is, precisely in the range in which the liner is supposed to absorb sound. While the instability wave itself is well documented, the mechanisms of sound amplification are comparatively less studied.

Liner instability has been investigated by several means. Theoretical works employ modal analysis including linear stability analysis and mode matching [20, 18, 10, 13, 21] or derive stability properties from the analysis of the Green's function. In the latter case, non-modal contributions can also be accounted for by doing an analysis of the critical layer, based on Frobenius expansions about critical points [22, 23]. An early prediction of instability [20] used a plug flow and the Myers boundary condition. The ill-posedness of the latter [24] raised doubts about the existence of the instability. However, other theoretical works get around this ill-posedness by considering a finite-thickness boundary layer [9, 25, 12] and confirmed that instability is possible. By contrast, taking into account viscosity but not the finite thickness of the boundary layer does not fix the ill-posedness issue [10]. Experiments based on microphone measurements and/or flow visualization techniques allowed to evidence an instability [6, 8, 17]. Different numerical methods have also been used to investigate its characteristics. The linearized Euler or Navier-Stokes equations can be solved either in the time domain [26, 27, 28, 29, 30] or the frequency domain [14] to characterize the instability as such [31, 14]. In the time domain, the instability, not being saturated by nonlinear effects can invade the simulation domain and affect the whole frequency range, so that its mitigation becomes necessary [32]. Given the hydrodynamic nature of the instability, it is appealing to perform the simulation of the flow over the acoustic liner by using the full Navier-Stokes equations, despite the computational cost it represents. Although not connected to acoustics, an early step in this direction was the incompressible simulation of the turbulent flow in a streamwise-periodic channel with porous walls [33], in which unstable waves were observed. The walls were modelled by transpiration surfaces having no resonance frequency. Simulations of a turbulent channel flow with the compressible Navier-Stokes equations and a model surface impedance possessing a resonance frequency [34, 16] also evidenced the presence of these unstable waves, which in addition were responsible for a drag increase. These simulations, while compressible, did not include any sound wave, either incident or liner-produced, due to the imposed streamwise periodicity. The aforementioned simulations employ a modeled impedance, but in the case of liners made of small cavities topped with a perforated sheet, it is possible to include the liner geometry in the simulation [35, 36, 37, 38]. This, amongst other, is necessary to account for the effect of the flow and nonlinearities on the acoustic impedance, but no instability has been studied with such resolved geometries yet. Tam et al [39] have reported an instability taking place in every liner cavity, but this kind of whistling is different from the surface mode considered here.

The objective of the present work is to perform the direct numerical simulation (DNS) of a turbulent channel flow with an acoustic liner on a portion of the wall, in which the flow is in spatial development, that is, there is no periodicity assumed in the streamwise direction. The compressible Navier-Sokes equations are computed and the liner is modeled by a surface impedance. While spatial simulations based on the linearized Euler equations are natural for sound propagation in ducts, they are less common for turbulent channel flow simulations. Compared to simulations that are streamwise periodic [34, 16], spatial channel simulations present several advantages. First, this better matches experimental situations as well as the physics, since instabilities develop in space. By contrast, for a streamwise periodic channel the instability develops in time, and while a comparison with a temporal linear stability analysis is possible it needs to be done during the short initial linear growth stage [16]. This is avoided in spatial simulations. Second, the spatial framework allows computing realistic sound waves, either incident or generated within the domain. Including sound waves to investigate their relation to the instability was an objective of the present work. The same geometric configuration as studied here was considered earlier using the linearized Euler equations [40] and the instability on the liner produced backpropagating sound waves that reinforced the instability; in the absence of saturation mechanisms, this feedback loop led to unlimited growth. The use of nonlinear equations in the present work is expected to provide a means to saturate the instability growth. Generally speaking, the nonlinear character can arise from the governing equations, but also from the impedance model itself, since resistance or admittance may be flow- or level-dependent [1]. Some models [41] or numerical implementations [42] include a nonlinear contribution in the impedance model. In the present work, the nonlinear character arises solely from the governing equations and the impedance model is linear to keep the problem simple. Note that the liner used in the experiments in [8], for which an instability was measured, is made of tightly spaced quarter-wavelength resonators without any face sheet, and does typically have a linear behaviour. This means that a linear impedance model coupled with nonlinear Navier-Stokes equations not only is a convenient model but also exists in practice. It is worth mentioning that some preliminary results for the present simulations were presented in [15]. Both the flow development and the non-reflective character were then unperfect at inflow, and it was feared that a possible retroaction loop could have affected the results. Hence, the strategy to simulate spatial flows has been improved to fix these issues [43], and the simulations with liner have been repeated as well as new ones performed. Despites many changes in the equations, boundary conditions, and forcing terms, the configurations shared between the present work and [15] are in agreement.

The organization of the paper is as follows. In section 2 we present the geometry of the channel, the governing equations and boundary conditions including the impedance law, the numerical methods, and list the different cases that are computed. In section 3 we present the simulation of a stable liner. The objective is to verify that the numerical model satisfactorily accounts for wave propagation in this situation. In section 4 we present the simulations of unstable liners, and also discuss the presence of sound waves. Finally, conclusions are given.

2 Geometry and numerical model

In this section we discuss the geometry of the channel, the model, and the numerical method. Except for the liner presence, methods are similar to those given in [43] which can be referred to for more details.

2.1 Geometry

We consider a turbulent channel flow with an acoustic impedance on a part of the bottom wall. The geometry is summarized in Fig. 1. The origin $(0, 0, 0)$ of the coordinate system is at point O. The channel walls are planes located at $y = \pm H$, where H is the channel half height (the full height is $L_y = 2H$). These planes are rigid except for a lined portion located in the bottom plane which is modeled by an impedance law. The liner leading edge is located at $x = x_L = 34.4H$, and the liner length in the streamwise direction is denoted by L. The flow is introduced at the inflow plane located at $x = 0$ and leaves the domain at the outflow at $x = L_x$. The domain length $L_x = 88H$ is the same for all simulations. Acoustic waves can eventually be injected at inflow, and both the inflow and outflow are non-reflective to plane acoustic waves coming from within the channel. Periodicity is used in the z-direction, and the length in that direction is $L_z \sim 4.2H$. Parameters specific to each of the simulations are presented in Section 2.6.

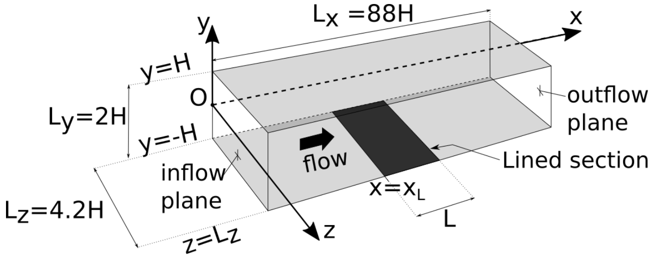

Figure 1: Geometry of the simulated channel (not to scale).

2.2 Governing equations

The flow in the channel is computed using the compressible Navier-Stokes equations [43]:

$$\frac{\partial \rho}{\partial t} + \frac{\partial \rho u_j}{\partial x_j} = 0 \tag{1}$$

$$\frac{\partial \rho u_i}{\partial t} + \frac{\partial \rho u_i u_j}{\partial x_j} + \frac{\partial p}{\partial x_i} = \frac{\partial \tau_{ij}}{\partial x_j} \tag{2}$$

$$\frac{\partial \rho s}{\partial t} + \frac{\partial \rho s u_j}{\partial x_j} = \frac{1}{T} \left(\Phi - \nabla \cdot \mathbf{q}\right) \tag{3}$$

where u_j for $j = 1, 2, 3$ are the components of the velocity vector $\mathbf{u} = [u\ v\ w]$, and ρ, p, s, T denote respectively density, pressure, entropy, and temperature. τ_{ij} are the components of the shear stress tensor $\boldsymbol{\tau}$. $\mathbf{q}$ is the heat flux, and $\Phi = \tau_{ij}(\partial u_i/\partial x_j)$ is the viscous dissipation function. To close the equations, we consider a thermodynamic ideal gas with equation of state $p = \rho r T$, where $r = 287\mathrm{JK}^{-1}\mathrm{kg}^{-1}$ is the ideal gas constant, as well as the following thermodynamic relation: $\mathrm{d}p = c^2 \mathrm{d}\rho + p/c_v \mathrm{d}s$. The speed of sound is $c = \sqrt{\gamma r T}$, and $\gamma = c_p/c_v$ is the heat capacity ratio, where $c_p = \gamma r/(\gamma - 1)$ and $\gamma = 1.4$ for air.

2.3 Boundary conditions

At inflow ($x = 0$) a developed turbulent flow is injected. It is computed by running a second simulation, called precursor simulation, of a rigid-walled channel using periodicity in the streamwise direction. At every time step, transverse planes of the precursor simulation feed the main simulation [43], which includes the acoustic liner. The precursor simulation is run at constant bulk density ρ_b and bulk velocity u_b, and has isothermal walls at temperature $T_{w,0}$, corresponding to sound speed $c_{w,0}$ and viscosity $\mu_{w,0}$. The Mach number and bulk Reynolds number defined by

$$M = u_b/c_{w,0} \qquad \mathrm{Re}_b = \frac{\rho_b u_b H}{\mu_{w,0}} \tag{4}$$

govern the precursor simulation, and also characterize the inflow conditions in the channel with liner. Another important quantity to characterize the flow is the friction Reynolds number:

$$\mathrm{Re}_\tau = \frac{\rho_w H u_\tau}{\mu_w} \tag{5}$$

where ρ_w is the wall mean density, μ_w the wall viscosity, and u_τ the wall friction velocity, defined from the wall friction τ_w by $u_\tau^2 = \tau_w/\rho_w$. ρ_w and u_τ are an outcome of the simulation and result from an average over z and t, they possibly depend on x. However, in the part of the channel located upstream of the liner Re_τ is streamwise independent and equal to its value in the precursor simulation. Hence, the value of Re_τ given below will also characterize the inflow. Technically, the flow is injected in the domain with the method of characteristics including a relaxation term [44, 45, 46]. This method is also used at outflow, where the unique ingoing characteristics is prescribed and relaxes the pressure to an imposed value. However, prior to relaxation plane wave masking [47] is used at both inflow and outflow to guarantee that plane acoustic waves leave the domain with minimal reflection [43]. Without such plane wave masking a mere relaxation would be reflective to plane waves at low frequency [48]. Regarding non-plane acoustic waves, the precise behaviour of the boundary condition would have to be assessed but it would certainly be partially reflecting. This is not a subject of concern in the simulations performed in this paper since no such non-plane waves hit the inflow or outflow boundaries. This is because the frequency of the acoustic waves present remain well below the first transverse mode cuton frequency and the distance between the inflow or outflow boundaries and the liner is large.

The boundary conditions at the walls need to be addressed. At the rigid walls, a no-slip condition on velocity is used: $u = v = w = 0$. At the lined wall, a simple mass-spring-damper model is employed, as in ref [16], which connects the wall normal velocity and pressure through [26, 16]:

$$M_L \frac{\mathrm{d}^2 v}{\mathrm{d}t^2} + K_L v + R_L \frac{\mathrm{d}v}{\mathrm{d}t} = -\frac{\mathrm{d}p}{\mathrm{d}t} \qquad y = -H, x_L \leq x \leq x_L + L \tag{6}$$

where R_L is the resistance, M_L is the mass, and K_L is the spring constant. This model accounts for one resonance frequency of the liner. The implementation of Eq. (6) differs from that in ref [16], since the governing equations are now written in conservative form, Eqs. (1-3), rather than in characteristic form. While the impedance boundary condition itself could still be written in characteristic form, a direct implementation has proven to be stable and is preferred here for its simplicity. Note that some stability issues with such a direct implementation have been reported, refer to the discussion in Section 2.3.2 of [16]. Hence, for example, Gabard and Brambley [30] report that a direct implementation is unstable and fix this by using a characteristic formulation. While the method of characteristics offers a systematic way to make the continuous problem well-posed, a problem with boundary conditions not written in characteristic form is not necessary ill-posed, as long as the direct imposition does not enforce outgoing characteristics or leave entering ones unspecified (see [49], pp. 359-365 and theorem 9.1.1). The convergence of our simulations indicate that we do not have such problems. The fact that some authors obtain unstable behaviours with direct imposition, and some others not, may be connected to the numerical implementation (boundary schemes used for example) since well-posedness can be destroyed by unstable numerical schemes. The implementation of Eq. (6) classically splits the equation into a first order system:

$$\begin{aligned} \frac{\mathrm{d}v}{\mathrm{d}t} &= Q \qquad (7) \\ \frac{\mathrm{d}Q}{\mathrm{d}t} &= \frac{1}{M_L}\left[-\frac{\mathrm{d}p}{\mathrm{d}t} - R_L Q - K_L v\right] \qquad (8) \end{aligned}$$

where Q is an auxiliary variable defined at the liner. It can be updated with $\partial p/\partial t$ in Eq. (8) written as:

$$\frac{\partial p}{\partial t} = c^2 \frac{\partial \rho}{\partial t} + \frac{\gamma p}{c_p}\frac{\partial s}{\partial t} = c^2 (1 - \frac{s}{c_p})\frac{\partial \rho}{\partial t} + \frac{c^2}{c_p}\frac{\partial \rho s}{\partial t}$$

where $\partial \rho/\partial t$ and $\partial \rho s/\partial t$ are obtained from Eq. (1) and Eq. (3). In the direct implementation, Eq. (7) is directly used to replace the wall-normal momentum equation (given by Eq. (2)) with:

$$\frac{\partial \rho v}{\partial t} = \rho Q + v\frac{\partial \rho}{\partial t}$$

at the liner boundary. This implementation has been validated on the same test case as in [16].
Some condition on temperature also needs to be imposed. The walls, both rigid and lined, are isothermal with a temperature that decreases linearly in x starting with value $T_{w,0}$ at $x = 0$. This is done to encourage a well-developed flow in the channel [43]. The Mach number is moderate in the present work ($M = 0.3$), and as a result the temperature drop between inflow and outflow is small, with a variation of about 3%. Temperature is not a variable that can be controlled directly but can be maintained at its initial value by enforcing the isothermal relation: $\partial s/\partial t = -(r/\rho)\partial \rho/\partial t$.

2.4 Numerical Schemes

The schemes are those used in [43]. The equations in skew-symmetric form [50] are discretized in a collocated manner using a finite difference method. The first derivatives are computed with a 6th order compact scheme for the central points, a centered 4th order compact scheme for the grid point next to the boundary, and a 3rd order compact upwind scheme at the boundary point. A similar pattern is followed for the second derivative. All these schemes are from [51]. Since the centered scheme is non-dissipative, a selective filter taken from [52] is used in general to avoid grid-to-grid oscillations. Finally, the time-advancement relies on a classical fourth-order four-step Runge-Kutta method.

2.5 Normalization

In the sequel, all quantities are specified in normalized form: lengths are normalized with H, density with ρ_b, flow speed with $c_{w,0}$, pressure with $\rho_b c_{w,0}^2$. The liner resistance, mass, and spring constant are normalized with $\rho_b c_{w,0}$, $\rho_b H$, and $\rho_b c_{w,0}^2/H$, respectively.

2.6 Configurations

The parameters for the different simulations are specified in Table 1. All simulations share the same domain size ($L_x = 88H$, $L_z = 4.18H$), and the same flow conditions (fixed Mach Number, $M = 0.3$, and fixed inflow friction Reynolds number, $\mathrm{Re}_\tau = 411$). They differ mainly by the characteristics of the liner and the liner length. The liner mass and spring do not vary from case to case, which fixes the radian resonance frequency of the liner:

$$\omega_r = \sqrt{\frac{K_L}{M_L}} \sim 0.37 \tag{9}$$

Case	R1	R023S	R035	R035f	R035S	R035L	R035SE
Re_b				6900			
M				0.3			
Re_τ (Re_τ^*)				411 (392)			
L_x/H				88			
L_z/H				4.18			
L/H	14.7	5.3	14.7	14.7	5.3	26.9	5.3
n_x	881	1181	1181	2001	1181	1181	1181
n_y	101	171	171	171	171	171	171
n_z	171	171	171	245	171	171	171
Δx^+	41	30	30	18	30	30	30
Δy_w^+	0.9	0.5	0.5	0.5	0.5	0.5	0.5
Δy_c^+	18.5	11	11	11	11	11	11
Δz^+	10	10	10	7	10	10	10
Δt	0.004	0.002	0.002	0.002	0.002	0.002	0.002
Nb iter	610e3	215e3	302e3	1e6	500e3	480e3	324e3
R_L	1	0.23	0.35	0.35	0.35	0.35	0.35
M_L				2.85			
K_L				0.39			
Injected waves	yes	no	no	no	no	no	yes

Table 1: Simulated Configurations.

This corresponds to an approximate value of frequency for peak sound absorption or for instability, even though the flow will modify this value. The liner resistance is varied so that the flow is stable ($R_L = 1$), convectively unstable ($R_L = 0.35$), or absolutely unstable ($R_L = 0.23$). These results about stability are specified in A. Three different liner lengths have also been used. Finally, some acoustic waves are eventually injected at the inflow of the simulation. This is the case for the stable liner (Case R1) in which wave absorption is investigated, and also for an unstable one (case R035SE).

Table 1 also provides the number of grid points (n_x, n_y, n_z), the corresponding mesh sizes (Δx, Δy, Δz), and the time step (Δt). The present simulations are coarsely resolved DNS, with a streamwise mesh resolution $\Delta x^+ \sim 30$ in most of the simulations, a spanwise resolution $\Delta z^+ \sim 10$, and a wall normal resolution ranging from $\Delta y_w^+ \sim 0.5$ at the wall to $\Delta y_c^+ \sim 11$ at the channel center (except for case R1 which is less resolved in the wall normal direction). In [16], a periodic simulation of ours was reported with similar resolution except $\Delta x^+ \sim 20$ for a liner having characteristics similar to case R023. A resolution $\Delta x^+ \sim 20$ was also used in coarsely-resolved DNS or well-resolved large-eddy simulation in [34] for a channel with impedance walls, in [53] for turbulent boundary layers with wall-suction or blowing, or in [52] for rigid walls with methods equivalent to ours. Using $\Delta x^+ = 30$ is expected to be slightly less precise and we accept this resolution here to limit the computational cost. In the physics involved, an instability develops along the liner, grows, and eventually breaks down into turbulence, as we will see. One might infer that the lack of precision is going to show up in this breakdown region on the liner. In order to verify the effect of the mesh size on the results, the simulation R035f, a refined version of R035, has been performed with $\Delta x^+ = 18, \Delta z^+ = 7$. A comparison between cases R035 and R035f is provided in B. This appendix shows that although some small quantitative differences exist, as expected, the physics is well calculated by our simulations using $\Delta x^+ = 30$.

To verify how good the flow arriving on the liner is, some statistics of the flow in the channel for case R035 are compared to reference data [54] for an incompressible flow at $\mathrm{Re}_\tau = 395$ in Fig. 2. The figure presents the mean streamwise velocity, the rms velocities, and the Reynolds stress for the precursor channel used to feed the spatial channel, for the spatial channel at a position upstream of the liner, and for the reference. Due to the non-negligible Mach number in our compressible simulation, $M = 0.3$, the relevant Reynolds number is the modified friction Reynolds $\mathrm{Re}^*_\tau = 392$, which agrees with $\mathrm{Re}_\tau = 395$ of the incompressible reference. The regular friction Reynolds number is $\mathrm{Re}_\tau = 411$. The + units used to represent the present simulations in Fig. 2 are actually $*$ units (see [43] and references therein for more details about this scaling). The figure shows that the incoming flow, if not perfect, is still very satisfying given the mesh resolution.

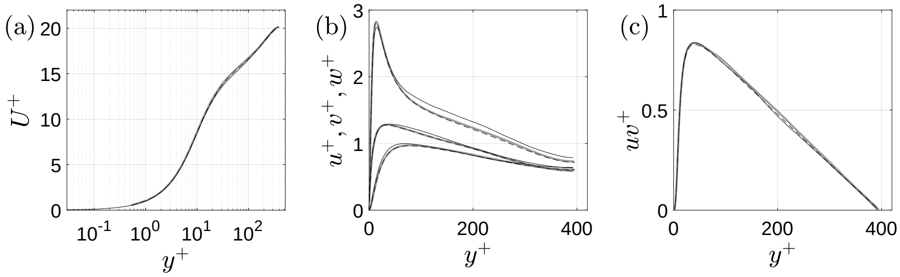

Figure 2: (a) Mean velocity profile ; (b) rms velocity; (c) Reynolds stress. —— Incompressible reference Moser; - - - precursor simulation; ━━ spatial simulation, upstream of the liner.

2.7 Probe recording

Apart from periodic savings of the whole flow field, recordings are performed at every time step at some probes located in the $z = 0$ plane. Prior to recording, the fields are averaged in the z-direction to increase the signal-to-noise ratio by averaging out turbulence [43]. This is justified because these probes are used to educe characteristics of plane acoustic waves or instability waves that are essentially two-dimensional, spanwise-independent. All n_y positions in y

are recorded. In the x-direction, probes are evenly spaced between $x/H \sim 20$ (upstream of the liner) and $x/H \sim 80$ (downstream of the liner): for case R1, there 200 probes with a step $\delta x/H = 0.3$. For the other cases, there are 270 probes with a step $\delta x/H = 0.22$. The probes are recorded every 40 time steps.

3 Stable liner

A stable liner is first considered. This is case R1 in table 1, which corresponds to the liner with resistance $R_L = 1$. The objective is to investigate if sound propagation and attenuation can be predicted with some accuracy when there is no instability. To do this, mode characteristics are educed from the simulations and compared to those given by a linear mode solver, which is the same as the solver used to compute the unstable modes in A.

The mean flow in the x-direction, U, is shown in Fig. 3, it results from averaging in time and in the homogeneous z-direction. It is mostly unaffected by the liner presence and remains independent of the streamwise position. The maximal value on the channel centerline is on the order of, and larger than, the imposed bulk Mach number at inlet, $M = 0.3$. Note that given the streamwise invariance of the flow, performing a local mode analysis is particularly relevant in this case.

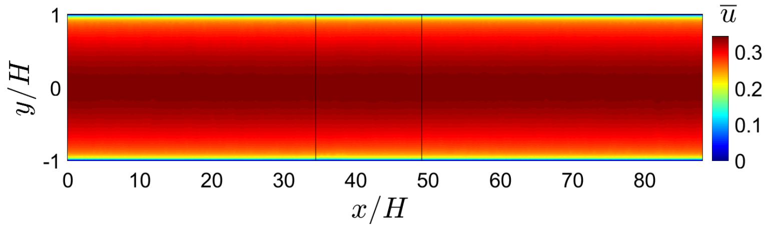

Figure 3: Mean streamwise velocity for case R1. Vertical lines indicates the liner limits.

Nine acoustic waves are sent at the inflow of the channel, they span a frequency range around the resonance frequency of the liner (given by Eq. (9)): $\omega_1 = 0.264$, $\omega_2 = 0.302$, $\omega_3 = 0.339$, $\omega_4 = 0.377$, $\omega_5 = 0.415$, $\omega_6 = 0.452$, $\omega_7 = 0.49$, $\omega_8 = 0.522$, $\omega_9 = 0.553$. Each incident wave has a sound pressure level of about 140 dB. A gross indication of the liner behavior is provided by the sound pressure level (SPL) at the probes located at the top wall of the channel. This is shown in Fig. 4(a) for each of the frequencies. The incident waves are partly reflected by the liner, which causes oscillations in the SPL in the part of the channel located upstream of the liner (oscillations are around the imposed incident value of 140 dB). The SPL drops in the lined section since the liner absorbs the waves, and reaches a flat plateau downstream of the liner (with

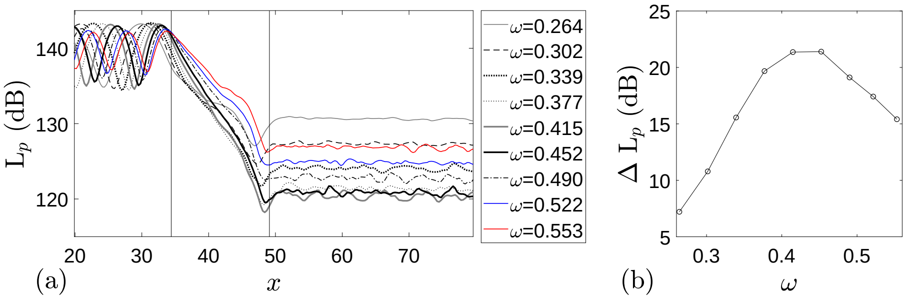

Figure 4: (a) Sound pressure level at the top channel wall ($y = 1$) as a function of streamwise position, for different frequencies. The vertical lines indicate the limits of the liner;(b) Sound attenuation by the liner as a function of the wave frequency. Case R1.

small fluctuations due to a lack of statistical convergence). This is a clue that the nonreflecting outflow boundary condition behaves properly. To verify this, a plane wave decomposition is performed in the downstream part of the channel in order to compute the reflection coefficient. Top wall pressure sensors are used to build and solve an overdetermined system for the downstream and upstream travelling plane acoustic waves [55]. The resulting reflection coefficient for plane waves is shown in Fig. 5. This remains below 3% over the frequency range. As explained in section 2.3 only plane waves reach the outflow boundary since the maximal radian frequency, ω_9, remains well below the cutoff frequency of the first transverse mode, whose value is about $\pi/2$ in our normalization. The difference of SPL between the incident acoustic wave and the transmitted one is shown in Fig. 4(b). Maximum attenuation occurs at the resonance frequency around $\omega \sim 0.43$ for which the SPL is decreased by about 21 dB.

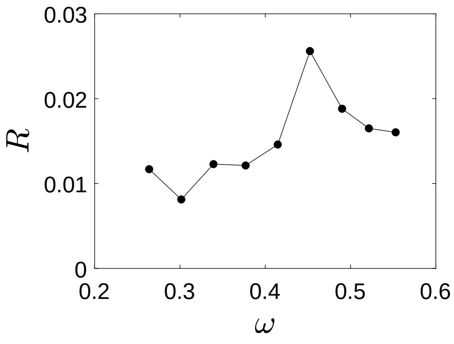

Figure 5: Reflection coefficient at the outflow. Case R1.

To characterize more precisely the propagation in the lined portion of the channel, we seek to compute the characteristics of the acoustic waves. A mode decomposition of the sound field in the lined portion of the channel can be written:

$$\begin{bmatrix} p(x,y,t) \\ u(x,y,t) \end{bmatrix} = \int \sum_n \begin{bmatrix} P_n(y,\omega) \\ U_n(y,\omega) \end{bmatrix} e^{\mathrm{i}(k_x^n(\omega)x - \omega t)} \frac{1}{2\pi} \mathrm{d}\omega \tag{10}$$

where only the pressure and streamwise velocity are included for brevity. This decomposition says that at each frequency ω, the field is a sum of modes indexed by n that have a streamwise wavenumber $k_x^n(\omega)$ and associated waveforms $P_n(y,\omega)$ and $U_n(y,\omega)$. The objective is to educe these values based on the recorded data $p(x_i, y_j, t_m)$ and $u(x_i, y_j, t_m)$ (probe positions where given in section 2.7) and compare them to our mode solver. In the Fourier domain, pressure in Eq. (10) becomes:

$$p(x,y,\omega) = \sum_n P_n(y,\omega) e^{\mathrm{i}k_x^n(\omega)x} \tag{11}$$

At given y and ω, this is a sum of complex exponentials in x, that is, a Prony decomposition. A Prony-like method can be used to educe the characteristics of these exponentials [56], as is often done in acoustic liner impedance eduction methods [57]. Here, the Matrix-Pencil method is used [58]. A first step requires Fourier transforming the recorded data, arranging them in two Hankel matrices, and solve an eigenvalue problem to find the values of k_x^n (Eqs(17-24) in ref [58]). Once these are obtained, the waveforms are found in a second step by solving a least square problem (Eq. (25) in ref [58]). To mitigate the effect of noise during the first step, rank reduction of the Hankel matrices is performed by eliminating singular values below a certain threshold [58]. The threshold value is presently computed using the strategy in [59]. The Prony decomposition concerns the x-direction, and here data at several y-positions are recorded. To take advantage of this, a multi-sensor analysis could be performed [56, 60]. Another option prefered here is to perform a Prony analysis for every y to find n_y estimations of k_x^n, identify clusters, and average each cluster to obtain a mean k_x^n. The standard deviation within each cluster provides an estimation of the error committed when computing k_x^n. This will be shown as an errorbar in the plots of the wavenumber.

The first step of the matrix pencil method is performed by using the pressure signal, which offers a better signal to noise ratio compared to velocity [43]. There are about 50 probes in the x-direction in the liner region $35 < x < 49$, leading to Hankel matrices of size 31×16. The singular value threshold [59] indicates a rank of 6, which provides 6 values of $k_x^n, n = 1...6$. Only 2 among the 6 values seem sufficiently robust, in the sense that k_x^n does not change too much in y. These wavenumbers are the right- and left-going acoustic modes, and are denoted $k^+(\omega)$ and $k^-(\omega)$, and we will focus only on them in the following. The second step, which uses the educed values of k^+ and k^-, is performed on both pressure and velocity at every y and provides the waveform for the downstream mode, denoted by $P^+(y,\omega)$ and $U^+(y,\omega)$, and those for the upstream mode,

denoted by $P^-(y,\omega)$ and $U^-(y,\omega)$.
The evolution of the educed wavenumber with frequency is presented in Fig. 6 for the downstream mode and is compared to the one obtained with a local modal analysis based on the computed mean flow. The agreement is very good, both on the real and imaginary part. The imaginary part, which corresponds to damping, peaks at the same frequency as the one for which the largest attenuation was observed in Fig. 4(b). The errorbar level is small, which means that this mode is found in a robust manner by the Prony method. The educed wavenumber for the upstream mode is shown in Fig. 7. This mode results from reflections at the trailing edge of the liner, and its damping rate is important, so that its amplitude is small compared to the downstream mode. As a result this mode is more difficult to detect, and this shows up in the larger errorbar. Despites this, both the real and imaginary part compare rather well to the mode solver result.

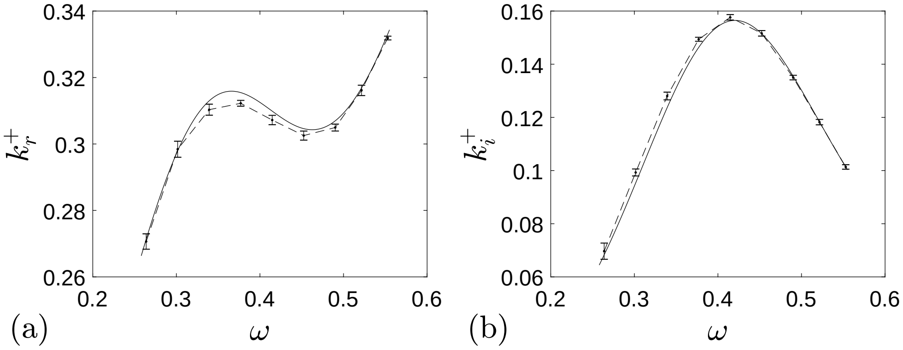

Figure 6: (a) Real part and (b) imaginary part of the wavenumber, k^+, of the downstream-propagating acoustic mode in the lined part of the channel: —— mode solver; - - - educed from the simulation with a Prony-like method. Case R1.

Waveforms of pressure and velocity are shown in Fig. 8 for $\omega = 0.52$. They compare reasonably well with the result returned by the local mode solver. The velocity for the upstream mode is somewhat noisy, with a peak value only computed approximately. Since the amplitude of the mode is small, it is difficult to separate it from noise, especially for velocity.

The streamwise reconstruction of pressure and velocity using the Prony decomposition, Eq. (11), is performed by taking into account in the sum either the downstream mode only, or both the downstream and upstream modes. The result is plotted as a function of x for some given distance to the wall in Fig. 9. It is seen that most of the amplitude is retrieved with the downstream mode only. The effect of the upstream mode is to increase the signal amplitude at the trailing edge of the liner ($x \sim 49$) where it is generated. This is particularly

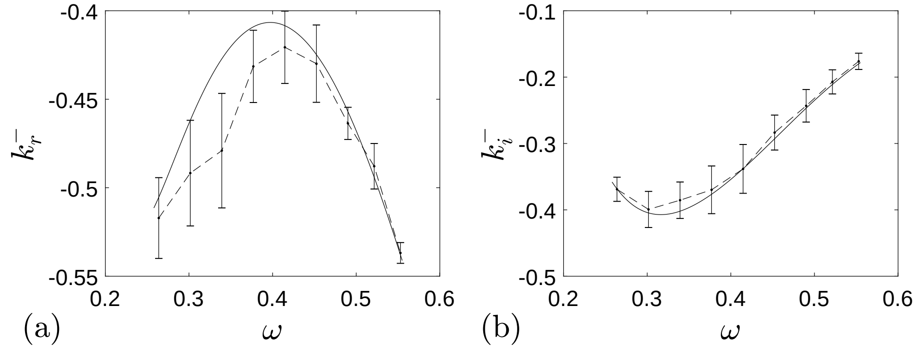

Figure 7: (a) Real part and (b) imaginary part of the wavenumber, k^-, of the upstream-propagating acoustic mode in the lined part of the channel: —— mode solver; - - - educed from the simulation with a Prony-like method. Case R1.

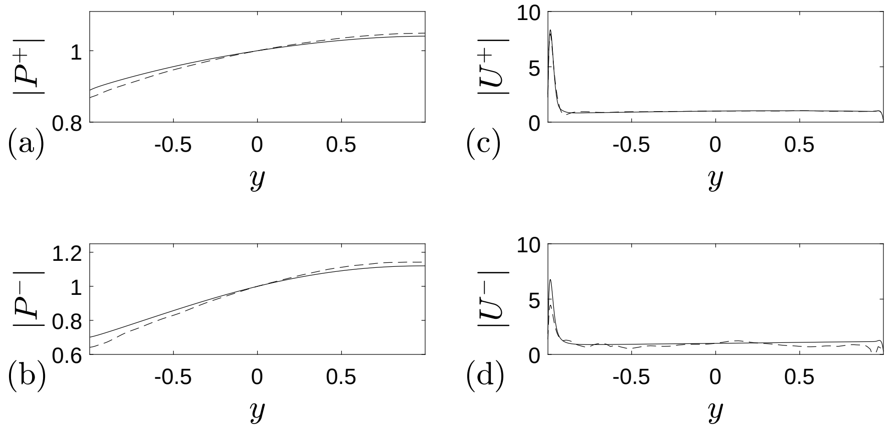

Figure 8: Modulus of the pressure waveform for (a) downstream- and (b) upstream-travelling acoustic mode in the lined part of the channel. Corresponding modulus of the velocity waveform for (c) downstream- and (d) upstream-travelling mode. For each curve, normalization is done by the pressure at $y = 0$. $\omega = 0.52$. Case R1.

seen in the pressure signal at $\omega \sim 0.26$ in Fig. 9(a). Hence, the upstream mode causes the SPL increasing at the liner trailing edge that is seen in Fig. 4(a). Figure 9(a) shows that the reconstruction with two modes is good for pressure, which is the reason why only these two modes are found by the algorithm. For velocity in Fig. 9(b), the reconstruction is much more noisy, which again is due

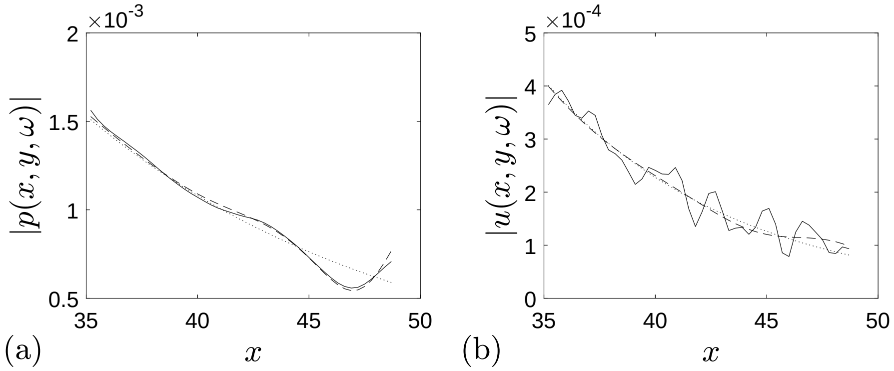

Figure 9: (a) Modulus of the pressure along the top wall ($y = 1$), for $\omega = 0.26$; (b) Modulus of the axial velocity (at $y \sim 0.99$), for $\omega = 0.52$. —— full signal recorded in the simulation, ····· reconstruction with only the downstream-travelling acoustic mode, – – – reconstruction with both the upstream- and downstream-travelling acoustic modes. Case R1.

to lower signal-to-turbulence ratio compared with pressure [43].

In conclusion, for a stable liner, the wave propagation in the lined region is computed in a satisfactory manner, with modes in agreement with those computed by a linear modal analysis based on the computed mean flow. In the next section we turn to unstable liners.

4 Unstable liner

4.1 Mean flow

We now consider the cases having a small enough resistance for the flow being unstable (see A). The mean flow for these cases is shown in Fig. 10. Contrary to the case R1 that was shown in Fig. 3, the mean flow is now disturbed in the vicinity of the liner, and the smaller the resistance the larger the disturbance, as seen by comparing Fig. 10(a) for $R = 0.23$ and Fig. 10(b) for $R = 0.35$. Figures 10 (b-d) correspond to the same liner resistance, $R = 0.35$, but a varying length of the liner. It is seen in Fig. 10(c) that the mean flow on the liner may have several low speed bumps in the vicinity of the liner before reaching eventually an established state, which seems to become the case in Fig. 10(d) for the longest liner, with $L/H = 26.9$.

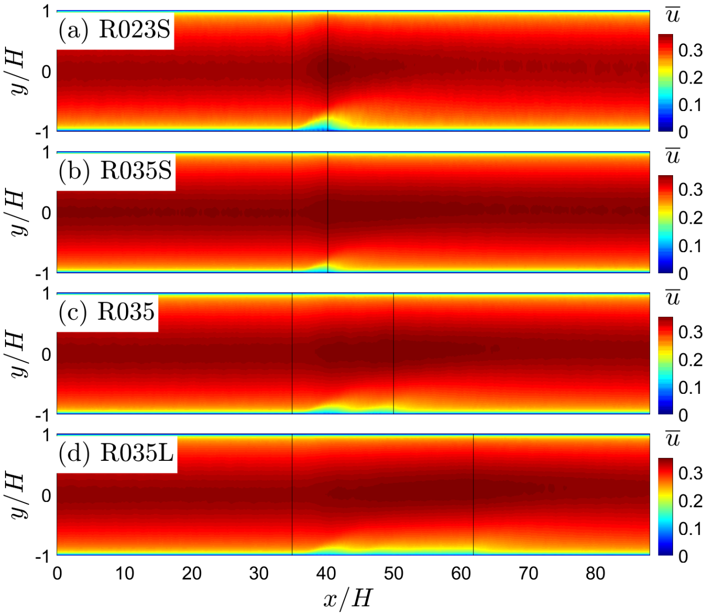

Figure 10: Mean streamwise velocity for cases: (a) R023S ; (b) R035S; (c) R035; (d) R035L. Vertical black lines indicate the liner limits. Axes not to scale.

4.2 Flow visualization

To complement the mean flow, an instantaneous visualization of the flow is shown in Figure 11 for case R035. We will focus on this case in the following, since qualitatively all cases have a similar development, except for the number of bumps on the liner, which depends on the liner length. The lined section, between $x = 34.45$ and $x = 49.1$, is indicated by a light white box. The back plane ($z = 0$) shows the streamwise velocity (u) which corresponds to a typical turbulent channel flow, the mean of which has been shown in Fig. 10(c) and also in Fig. 2. Half of the bottom plane represents the streamwise velocity at $y = -0.98$ (in wall units, $y^+ \sim 8$), the other half represents the wall-normal velocity (v) at $y = -1$. The latter is zero outside the lined section due to the rigid wall boundary condition at the channel wall. Both components of the velocity show a wave above the liner, rooted in the unstable behavior. Figure 12 presents a zoom of the previous figure in the lined region only. In the upstream part of the liner, $35 < x < 36$, the liner has not modified significantly the incident flow and one can see the near-wall streaky structure in the u-component. Follows a first region of instability for $36 < x < 42$ where the instability grows and saturates, leading to a modified mean flow. In an intermediate region, $42 < x < 44$ the unstable wave tends to disappear while the mean flow reattaches to the wall around $x = 44$, according to Fig. 10(c). The disappearance of the wave

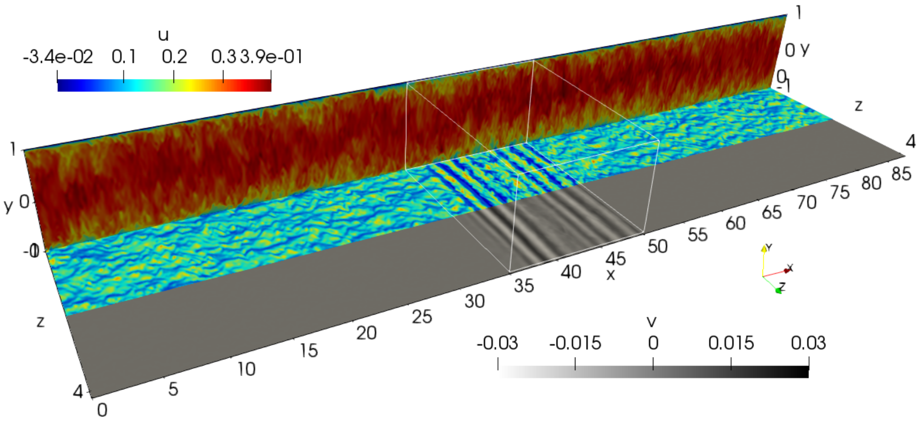

Figure 11: Instantaneous flow visualization. Case R035.

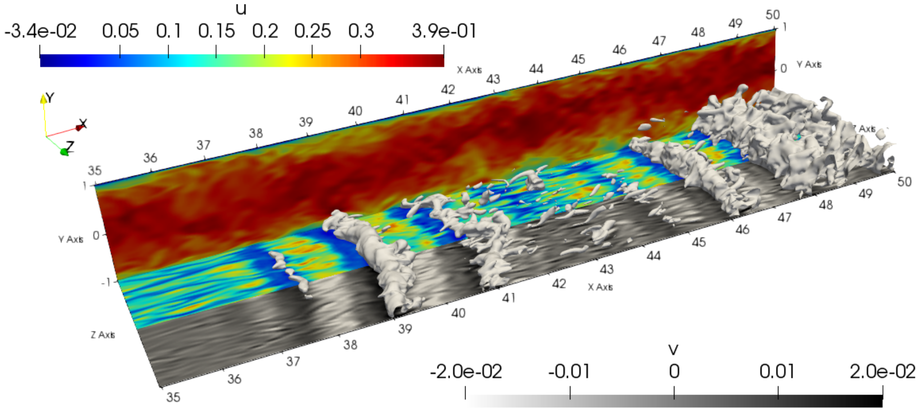

Figure 12: Zoom in of Fig. 11 in the lined section. White surfaces indicate a pressure isoncontour. Case R035.

in $42 < x < 44$ is not due the wave becoming linearly damped, but rather to its breakdown into turbulence. Indeed, the linear stability analysis presented below in Section 4.3 shows that the local mean flow profiles are unstable for any streamwise position along the liner and that the wave has a positive growth rate. In its initial stage, the wave grows quickly, reaching large amplitudes. A typical saturation amplitude is 0.015, as seen in Fig. 12, which is about 5% of the center velocity. At the liner surface, this corresponds to a normal displacement $d_a^+ \sim 15$. This important wall-normal motion promotes the generation of vortices and the breakdown of the wave into turbulence. Figure 13(a) shows an instantaneous top view of isoconcontours of the Q-criterion (colored by wall normal velocity) showing the presence of vortices. Their number increases importantly in the saturation region of the unstable wave. In the zoom shown in Fig. 13(b) it is seen that the vortices are concentrated in the region where the normal velocity changes from positive to negative (isocontours are colored in red and then in blue as one moves in the streamwise direction), that is, where blowing is followed by suction. This region also shows many hairpin-like or ring-like vortices that are commonly observed in boundary layer transition [61, 62]. Due to the large wall normal velocity, and the incident flow being fully turbulent, the breakdown is violent, and the amplitude of the wave decreases rapidly in less than two wave lengths. Following this breakdown, the mean flow is modified, but is still unstable according to the analysis in Section 4.3, even if the growth rate decreases. As a result, a second instability is taking place for $44 < x < 49.1$. Of course this region would not be observed for a shorter liner (case R035S), and could evolve downstream for a longer liner (case R035L). What has been referred to above as bumps are successive instability regions. Downstream of the liner, the vortices created on the liner do not survive, and a return to normal is approximately observed at a distance $6H$ from the liner trailing edge. This will also be confirmed from the plots in Fig. 25 and Fig. B.3 which show that Re_τ retrieves its nominal value within $10H$ from the liner trailing edge.

To assess how fields vary in time, a time-space plot of pressure at $y/H = -0.96$ is shown in Fig. 14. Pressure is averaged in the z-direction, and detrended to remove the mean pressure drop in the x-direction. The two regions of instability are seen, with peak amplitudes at $x \sim 40$ and $x \sim 48$, respectively. The amplitude in the first region is larger than the one in the second region. The first region oscillations in particular are very stable in time, which has been observed for all computed cases. While such a clean auto-oscillation is expected for an absolutely unstable flow possibly acting as an oscillator (R023), it was not expected to occur in the absence of any acoustic excitation for a convectively unstable flow such as R035. The resistance $R_L = 0.35$ is not much larger than the threshold value, $R_L \sim 0.3$, below which there is absolute instability (see Fig. A.3). We have performed a simulation for a less unstable resistance (far from the threshold), $R_L = 0.5$, not listed in table 1, and the same auto-oscillation occurred (not shown). We conclude that there must be a retroaction loop by a left-propagating acoustic wave generated at the trailing edge of the liner. Such a feedback loop has been observed in linear simulations [40] and also confirmed by global linear stability analyses [63]. This point will deserve further investigation in the future, and we will also come back to it in a subsequent section below. Also shown in Fig. 14 are lines whose slopes are respectively the flow speed, the right-going acoustic wave speed in rigid-walled sections, and the instability phase speed, as computed in the next section. Downstream of the liner $x \geq 49.1$, we observe pressure ridges in the $x - t$ plane that are aligned with the acoustic speed, showing that some acoustic waves are generated by the liner. In the following sections, we present more details on the instability wave and on the acoustic wave.

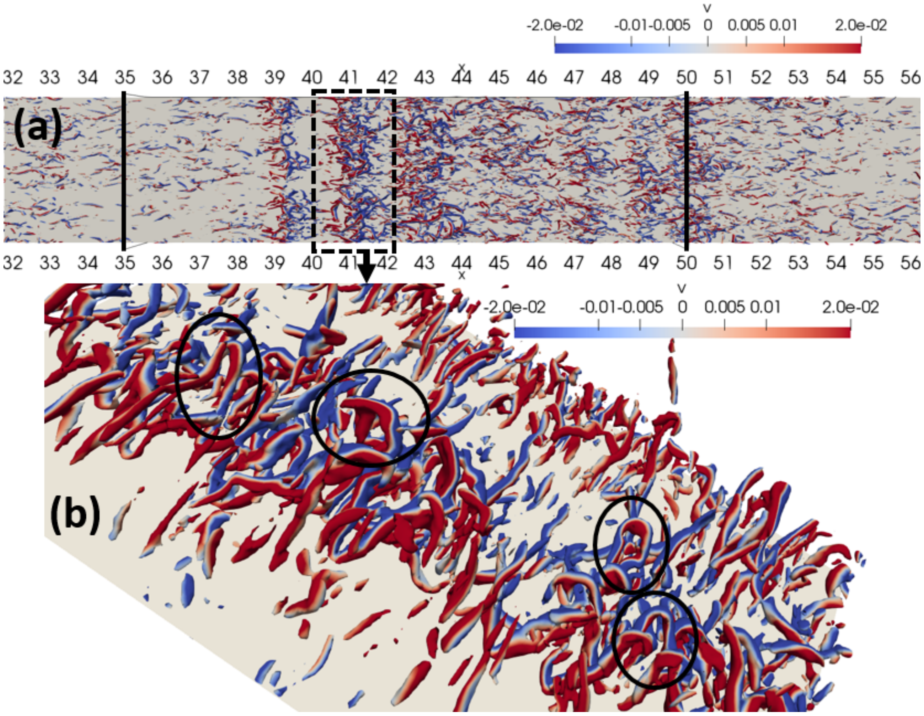

Figure 13: Isocontours of Q-criterion, colored with the wall-normal velocity. (a) Top view (shown plane is x-z plane) with thick vertical lines indicating the liner limits; (b) zoom in of the region around $x \sim 41$ indicated by a dashed box in (a). Circles indicate hairpin-like vortices. Case R035.

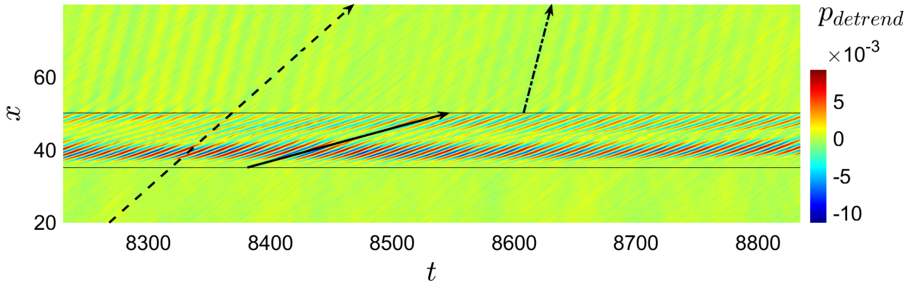

Figure 14: Time-space diagram of (detrended) pressure at $y/H = -0.96$. Case R035. - - - flow speed (slope M); -·- right-going plane acoustic wave speed (slope $(1 + M)$); —— instability phase speed. Arrows indicate the directions of propagation. The two thin horizontal lines mark the limit of the lined region.

4.3 Instability

In this section, the simulation results are used to compute the characteristics of the observed instability, which are then compared with predictions from a linear local stability analysis based on the computed mean flow.
The frequency at which oscillations are taking place is first identified. Figure 15 plots the near wall pressure spectrum at two points located in each of the instability regions: $x \sim 37$ in the first region, $x \sim 47.2$ in the second region. The frequencies for maximum oscillation amplitude are close but different in the two regions: $\omega \sim 0.43$ in the first, $\omega \sim 0.41$ in the second. This change in the maximally amplified frequency results from the mean flow being modified downstream of the first instability breakdown. To see to what extent the physics in these regions is governed by linear physics (such as a linear instability) the coherence, as defined on p. 172 of [64], is plotted at the frequency of the instability between several sensor pairs in Fig. 16 ($\omega = 0.43$ is shown and $\omega = 0.41$ gives similar plots). In Fig. 16(a) the coherence between the wall normal velocities at any two points on the liner ($y = -1$, $35 < x < 50$) is shown. Overall, two different coherent regions corresponding to the two instabilities are observed (with respective locations $35 < x < 43$ and $43 < x < 50$). The coherence between these regions is not completely negligible, as seen in Fig. 16(b), which presents two cuts of the former color map at two positions, each located in one of the unstable regions. For example, the coherence between the wall-normal velocity on the liner and that at a reference point located in the second unstable regions does not completely vanish in the first region. This is a clue that despite the first instability breakdown, some perturbations in the unstable frequency range reach the second instability region where they are amplified. Figure 16(c) presents the coherence map between the near wall wall-normal velocity, and the pressure on the top wall. It appears that the pressure downstream of the liner is mainly coherent with the velocity at the very end of the liner. This will be developped below.

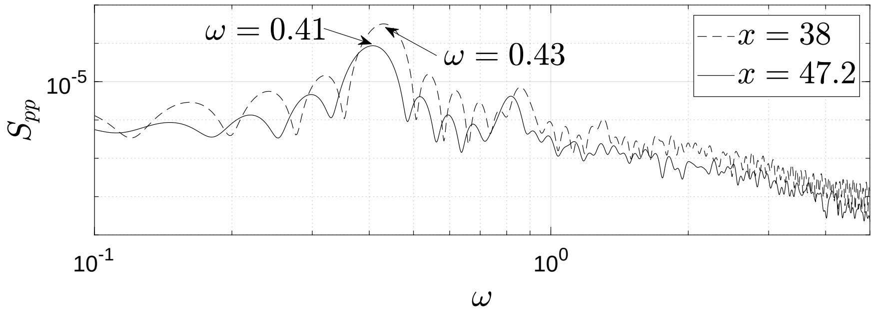

Figure 15: Spectrum of pressure obtained at $y = -0.96$ for: - - - $x \sim 37$ (first growth region); —— $x \sim 47.2$ (second growth region).

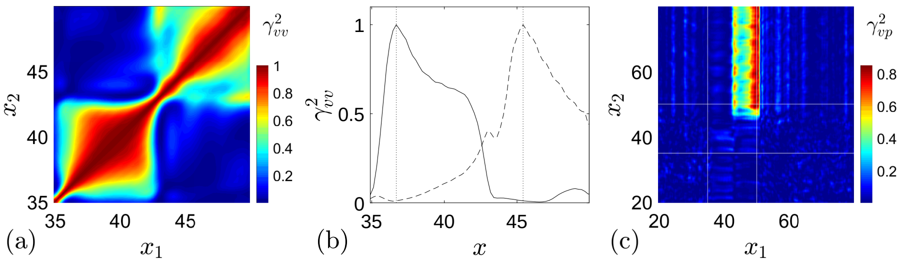

Figure 16: For a given angular frequency $\omega = 0.43$: (a) Map of coherence $\gamma^2_{v(x_1)v(x_2)}$ between $v(x_1)$ and $v(x_2)$, both taken on the bottom wall ($y = -1$). (b) —— Coherence between $v(x)$ and $v(x_a)$ at a reference location $x_a = 36.7$ located in the first growth region (both at $y = -1$); - - - Coherence between $v(x)$ and $v(x_b)$ at a reference location $x_b = 45.4$ in the second growth region (both at $y = -1$). (c) Map of coherence $\gamma^2_{v(x_1)p(x_2)}$ between $v(x_1)$ at $y = -0.94$ and $p(x_2)$ at y=1 (top wall); thin white lines indicate the liner limits. Case R035.

We need to obtain the wavenumber $k = k_r + \mathrm{i}k_i$ of the instability, described by $e^{\mathrm{i}(kx-\omega t)}$, see A. To do this, we obtain the complex amplitude of the instability in each of the regions at the observed frequency, and make a fit to obtain k. Since there is no external excitation, the amplitude is computed with respect to a reference probe at x_0. Using a cross spectrum between the sensor at x_0 and the one at x, and denoting by H the transfer function between these two locations, we compute: $H(x, \omega) = S_{x_0 x}(\omega)/S_{x_0 x_0}(\omega)$, where the spectra S_{xx} can be computed at any wall normal location (y) and for any variable. In addition, H has to be: $H(x, \omega) = e^{\mathrm{i}k(\omega)(x-x_0)}$. Hence a fitting of H as a function of x provides k. Actually, we fit a scaled version of H which corresponds to the wave amplitude: $A(x, \omega) = \sqrt{S_{x_0 x_0}} H(x, \omega)$. Figure 17 shows a fit of the modulus $A(x, \omega)$ for pressure close to the liner ($y = -0.96$) and at frequency of maximum oscillation amplitude, $\omega = 0.43$. The synchronization position is $x_0/H = 36$. $A(x, \omega)$ is meaningful only for the positions x shown in the figure, for which the coherence between x_0 and x is large (this does not encompass the second region). In this region, a linear trend is found corresponding to exponential growth, and the fit to this region is shown. This provides k_i and a fit to the phase (not shown) provides k_r. Overall, the fit in the first region of instability gives: $k = 4.8 - 2.2i$. An equivalent fit in the second region (not shown) gives : $k = 4 - 0.6i$.

These frequencies and wavenumbers are now compared to those predicted by a linear stability analysis. For the first growth region, the fit region is centered at $x = 36$. Hence, we perform the local stability analysis using the mean

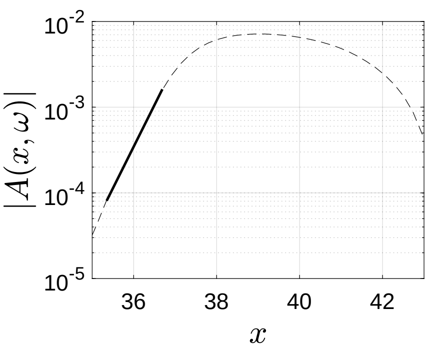

Figure 17: Fit of the amplitude of pressure in the first unstable region: - - - $A(x,\omega)$; ▬ fit. $y/H = -0.96$. $\omega = 0.43$.

velocity profile at this position and calculate the unstable mode as a function of frequency. Figure 18 presents the variation of the surface mode wavenumber with frequency. The educed one as obtained above is shown as a symbol in the

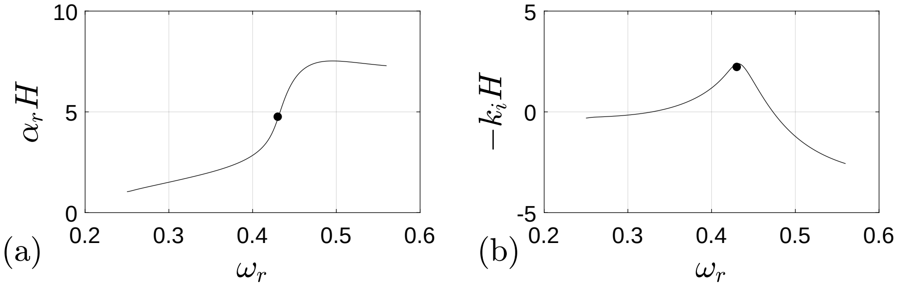

Figure 18: Wave number of the surface mode versus frequency. (a) real part; (b) imaginary part. —— obtained with a local stability analysis based on the mean flow profile at $x \sim 36H$; ● postprocessing of numerical simulations (fit around $x \sim 36H$).

figure, it is found to fall on the stability curve, and corresponds to the most amplified mode, that is, the one having the largest value of -k_i in Fig. 18(b). Thus, the observed instability frequency and wavenumber match the ones computed with a local linear stability analysis based on the actual mean flow profile. In addition, Fig. 19 shows that the waveforms associated with the instability, extracted from the simulation at $x \sim 37$ (at the end of the first exponential region), are also in agreement with the ones computed by using the linear stability analysis.

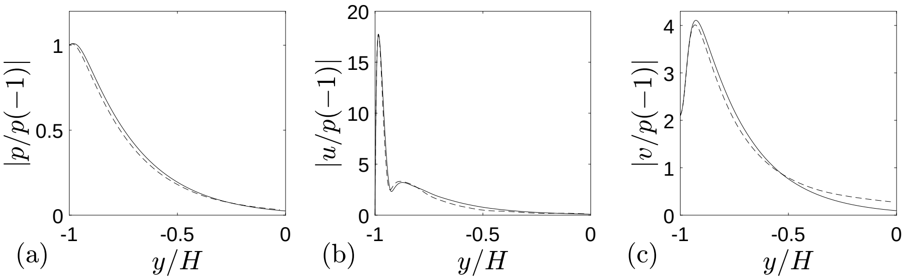

Figure 19: y-profiles of the instability. Norm of: (a) pressure; (b) axial velocity; (c) wall-normal velocity. —— obtained from mode solver; - - - from simulation.

The stability analysis has been repeated at several streamwise positions along the liner and the characteristics of the unstable mode are shown in Fig. 20. Two growth regions are identified by the stability analysis, since there are two peaks in the growth rate, one at $x \sim 36$, the other at $x \sim 45$. The second growth is weaker than the first one. It also has a smaller angular frequency (0.41 versus 0.43 for the first region) and a smaller real part of the wavenumber (3.8 versus 4.7). These variations are observed in the unstable waves observed in the simulation (symbols). Hence, a local analysis based on the local computed mean flow profile accounts for most of the phenomena observed in the liner region.

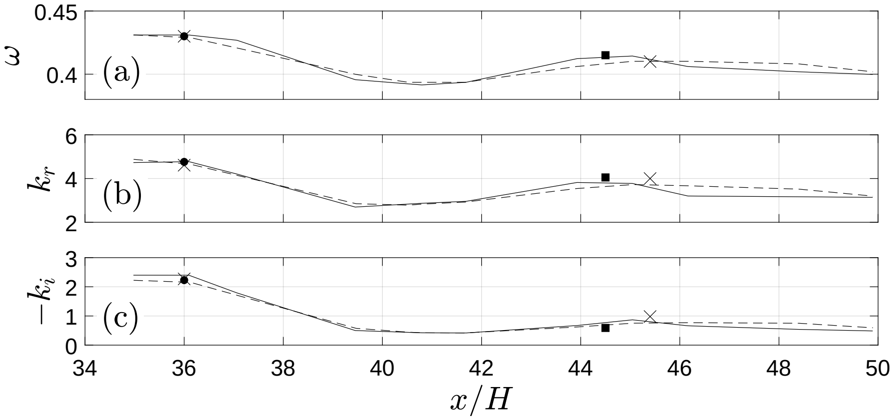

Figure 20: Characteristics of the instability having maximal growth rate at each streamwise station for case R035 : (a) ω; (b) k_r; (c) $-k_i$ (growth rate). —— local stability analysis based on the computed mean flow at x; ● characteristics educed in the first unstable region ; ■ characteristics educed in the second unstable region. Also shown with dashed lines and × symbols are the results obtained for case R035f.

For a longer liner, the growth rate would eventually vanish, and the flow reach a developed state, as Fig. 10(d) seems to indicate.

4.4 Acoustic wave generated by the liner

In this section, the presence of acoustic waves is discussed. These waves were evidenced in Fig. 14 in the downstream part of the channel past the liner. A time-space diagram of the pressure but now at the top rigid wall of the channel and for case R035S is shown in Fig. 21. Case R035S corresponds to a shorter liner, which behaves just as the longer one but has only one region of instability on the liner, with an observed (and predicted) oscillation at $\omega = 0.43$. Several wave speeds are indicated by arrows in the figure (when they depend on frequency, they are computed for $\omega = 0.43$). The instability phase speed has no signature in the upper plane (the instability wave is seen only close enough to the liner, as in Fig. 14). However, acoustic waves are clearly seen downstream of the liner, moving with speed $(1 + M)$, and also upstream of the liner, moving with speed $-(1 - M)$. These waves are emitted by the liner. In the lined section, and particularly near the trailing edge of the liner, that is for $38 < x < 40$, another acoustic wave is seen, the crests of which are connected to those of the acoustic wave past the liner. The right-going and left-going plane acoustic waves in the lined section can be computed by the mode solver, based on the mean flow. Unlike the instability, their wavenumbers are almost independent of this flow and thus of the streamwise location on the liner. At $\omega = 0.43$ the wavenumber for the downstream acoustic wave is $k^+ = k_r^+ + \mathrm{i}k_i^+ \sim 0.23 + 0.35\mathrm{i}$, and for the upstream acoustic wave it is $k^- = k_r^- + \mathrm{i}k_i^- \sim -0.22 - 0.42\mathrm{i}$. The imaginary part corresponds to damping by the liner. The short arrow in

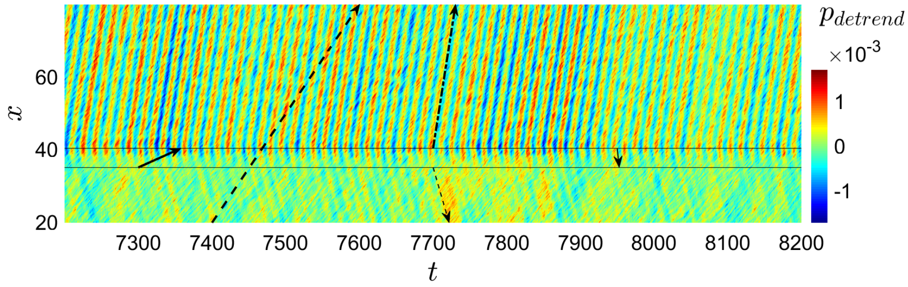

Figure 21: Time-space diagram of (detrended) pressure at the top wall, $y/H = 1$. Case R035S. ━ ━ ━ flow speed (slope M); ━━ instability phase speed; ━·━ right-going plane acoustic wave speed (slope $(1 + M)$); - - - left-going plane acoustic wave speed (slope $-(1 - M)$); —— on-liner left-going acoustic wave speed (slope ω/k_r^- and $\omega = 0.43$). Arrows indicate the directions of propagation. The two horizontal lines mark the limit of the lined region.

the lined region in Fig. 21 corresponds to the phase speed ω/k_r^-, it is aligned with the wave crests in the vicinity of the liner trailing edge. Thus, this wave is generated at the liner trailing edge and travels upstream while being damped.

The sound pressure level at $\omega = 0.43$ is plotted in Fig. 22 versus the streamwise distance counted from the liner trailing edge, for cases corresponding to different liner lengths, R035S, R035, and R035L. In all three cases, an acoustic wave is produced by the liner and observed downstream of it. However, the wave has a larger pressure level for the shortest liner ($\sim$ 132 dB) than for the other two, which have a comparable level downstream ($\sim$ 124 dB). A plane wave decomposition in the rigid-walled part of the channel located downstream of the liner has been performed to confirm that these pressure levels are indeed connected to plane acoustic waves. In the lined section, the pressure level decreases from the liner trailing edge, and the damping rate appears to be governed by k_i^- (thick dashed line). Hence, it seems that the acoustic waves are generated at the liner trailing edge by the scattering of the instability. In particular, they are not produced along with the instability as the latter grows. For the short liner, there is only one instability region. For a long liner, there are several successive instabilities, but only the last one, which crosses the liner trailing edge, is scattered into sound. The last region corresponds to a smaller instability amplitude compared with the first one (as discussed in connection with

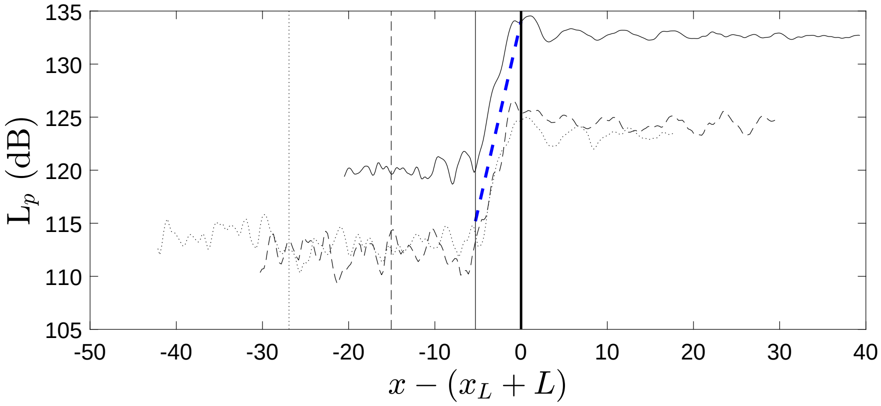

Figure 22: Pressure level along the top wall ($y = 1$) vs streamwise distance counted from the liner trailing edge, at $\omega = 0.43$: —— short liner (R035S); – – – nominal liner (R035); ····· long liner (R035L). The thick vertical line indicates the position of the liner trailing edge. The other vertical lines indicates the different liner leading edge positions and their line styles match the corresponding curves. The thick dashed line (- - -) indicates the decay rate of the acoustic wave travelling upstream, it is computed from k_i^-.

Fig. 14). This explains why the short liner emits more sound than the longer ones: this is because the amplitude of the scattered instability is larger. In addition, the shortest liner also produces a non-negligible sound level (~ 120 dB) upstream of the liner. This is connected to the upstream-travelling acoustic wave generated at the liner trailing edge, which is not completely absorbed by the short liner, and leaves the liner through the leading edge. This acoustic wave in the part of the channel upstream of the liner was observed in Fig. 21.

It has been conjectured in section 4.2 that an organized oscillation on the liner for $R_L = 0.35$ (corresponding to convective instability) is likely due to some feedback by acoustic waves. Figure 22 shows that for a short liner (R035S) the acoustic wave emitted at the liner trailing edge reaches the leading edge with a non-negligible amplitude (~ 120 dB). For longer liners, R035 and R035L, this wave is damped over a longer distance and its amplitude at the liner leading edge is much smaller, so that it is less likely to trigger instability. Figure 23 shows a time-space diagram of pressure for the longest liner. This shows that the instabilities on this liner are sustained but in a more intermittent fashion compared with shorter liners, R035 (see Fig. 14) or R035S (not shown). This tends to back the conjecture above.

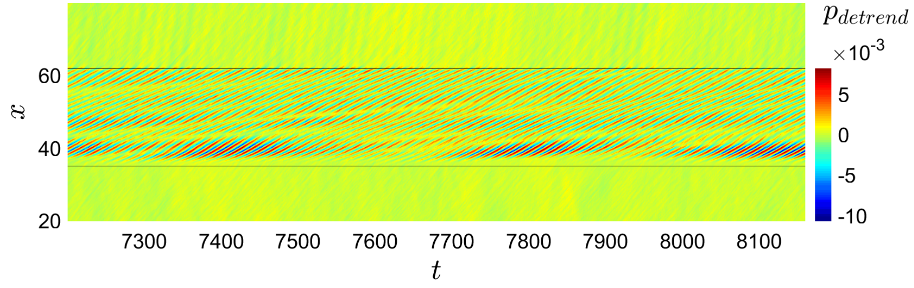

Figure 23: Time-space diagram of (detrended) pressure at $y/H = -0.96$. Case R035L. Horizontal lines indicate the liner limits.

4.5 Effect of acoustic excitation

Finally, the effect of an incident acoustic wave is briefly discussed. In reference [8], experiments were conducted with an unstable liner. It was observed that the instability was more likely to be sustained in the presence of an incident acoustic wave with frequency matching that of the instability. In addition, the acoustic waves were sometimes amplified by the instability, instead of being damped by the liner. In the present simulations, flow conditions and the liner differ from that in the experiments, and the previous section has shown that the instability could be sustained without incident wave. However, we still would like to know what the effect of an incident wave is. To answer this question we have run case R035SE in table 1, which uses the same short liner as case R035S, but a plane acoustic wave is sent at the inflow. The level of the incident wave is 140 dB, and its frequency is the same as the instability ($\omega = 0.43$). If there were no instability, this frequency would correspond to peak acoustic absorption by the liner. Acoustic wave absorption was shown in Fig. 6(b) for $R_L = 1$, and it follows the same trend for $R_L = 0.35$ (not shown), just with different wavenumber values. Acoustic wavenumbers at $\omega = 0.43$ for $R_L = 0.35$ were specified in the previous section (these are recalled: $k^+ = k_r^+ + \mathrm{i}k_i^+ \sim 0.23 + 0.35\mathrm{i}$, $k^- = k_r^- + \mathrm{i}k_i^- \sim -0.22 - 0.42\mathrm{i}$).

The mean flow in the vicinity of the liner is first considered. It is shown with and without acoustic excitation in Fig. 24. It it seen that the mean flow perturbation occurs more rapidly with acoustic excitation, which means that the instability starts developing at a more upstream position. Figure 25 shows the friction Reynolds number at the bottom wall of the channel. Upstream of the liner, the Reynolds number at the rigid wall takes its target value (~ 411), as discussed in section 2.6. As a result of the instability, as for simulations with streamwise periodicity [16], the friction increases on the liner, with Re_τ up to 800. Again, the effect of acoustic excitation is to trigger this increase at a more upstream position on the liner. However, the maximum increase in friction is just slightly larger than without incident wave. Finally, Figure 26 shows the sound pressure level at the top wall of the channel, at frequency $\omega = 0.43$. The curve for case R035S is the same as in Fig. 22, and the acoustic level downstream or upstream of the liner is produced by the liner due to the instability. For case R035SE with incident wave, the acoustic level upstream of the liner is mostly due to the injected wave, and a standing wave pattern is seen. Downstream of the liner, the acoustic level is about the same as without acoustic excitation

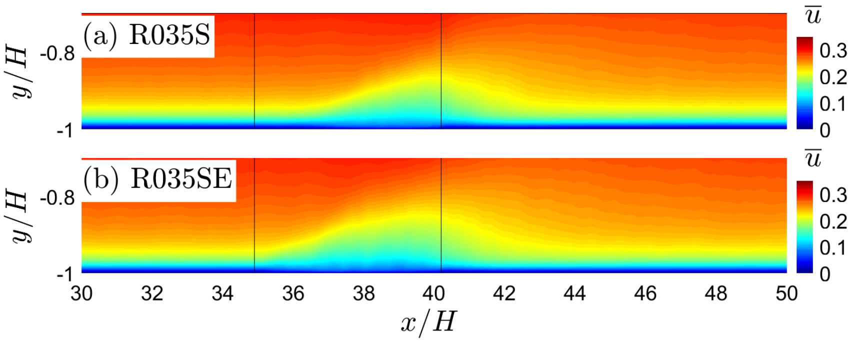

Figure 24: Mean velocity in the x-direction in the vicinity of the bottom wall: (a) case R035S (without incident acoustic wave); (b) case R035SE (with incident acoustic wave). Vertical lines mark the liner limits.

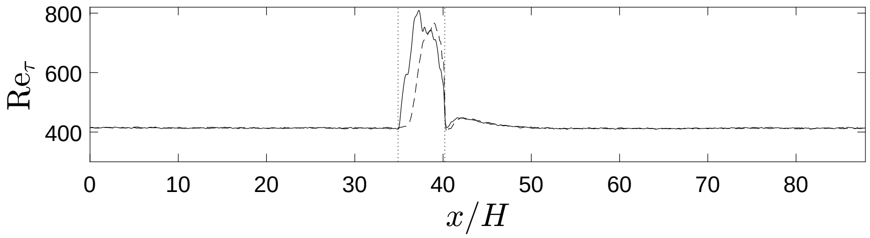

Figure 25: Mean friction Reynolds number at the bottom wall: —— case R035SE (with incident acoustic wave) – – – R035S (without incident acoustic wave). Vertical lines indicate the liner limits.

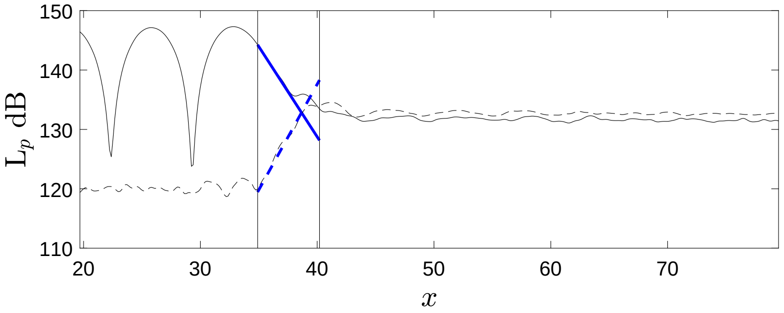

Figure 26: Sound pressure level at top wall. —— case R035SE; - - - case R035. The thick lines indicate the rate of decay of the acoustic wave travelling upstream (– – –) and of the one travelling downstream (——). Vertical lines indicate the liner limits.

($\sim$ 132 dB). On the liner it appears that the incident sound wave is damped, and the damping rate corresponds to the one of the right-going acoustic wave (computed from k_i^+ and shown as a thick plain line). It reaches a plateau at the trailing edge of the liner ($38 < x < 40$) probably due to the wave travelling back from the liner extremity. The acoustic wave generated downstream is then a product of the instability, and is not connected directly to the incident wave, the latter being absorbed normally by the liner.

The conclusion of this and the previous section is the following. In the experiments reported in [8], the convectively unstable liner was oscillating in a sustained manner only under the action of incident acoustic waves. These waves were amplified by the liner rather than damped when their frequency was in the unstable range, which is also the acoustic absorption range. In the present simulations, with different flow conditions and liner characteristics, the instability is sustained even without incident waves. This is likely due to the feedback loop by the acoustic wave generated at the liner trailing edge by scattering of the instability wave. With longer liners than those simulated here, which would absorb the backpropagating acoustic wave over a longer distance and reduce its amplitude, it is possible that this feedback loop would be suppressed, and the instability would be observed only with incident waves, as in the experiments. The scattering of the instability at the liner trailing edge also produces an acoustic wave downstream of the liner. The effect of an incident acoustic wave is to move the triggering point of the instability upstream compared with the unexcited case. This results in a modification of the mean flow on the liner, and increases slightly the friction, but the effect is less spectacular than if the incident wave were triggering the instability rather than moving it upstream. The incident acoustic wave is indeed absorbed by the liner, and the downstream propagating acoustic wave is again due to the scattering of the instability by the liner trailing edge, that is, it is not directly connected to the incident wave. In the case considered here, R035SE, the incident acoustic wave has a level of 140 dB, and the emitted wave level is 132 dB. Hence, the incident wave is not amplified, it is just not as damped as is would be without instability. However, it is inferred that if the incident level had been 120 dB, the downstream level would still have been 132 dB, giving the impression that the incident wave is amplified. All in all, the behaviors observed in the simulations are of a similar nature as those observed experimentally.

5 Conclusion

The direct numerical simulation of a spatially developing turbulent channel flow at $\mathrm{Re}_\tau \sim 400$ has been performed, in which a part of the bottom wall is covered with an impedance representing an acoustic liner. The flow incident on the liner is computed in a precursor simulation and is fully developed. Depending on its resistance, the acoustic liner can be stable, convectively unstable, or absolutely unstable, based on a local spatial linear stability analysis using as base flow the simulated mean flow.

A stable liner has first been computed, excited by several incident plane acoustic waves having frequencies from below to above the liner resonance frequency. Acoustic propagation and absorption by the liner have been verified by comparing the educed wavenumbers and wave shapes to those predicted by the linear mode solver.

Unstable liners have then been computed, with a special focus on convectively unstable liners with resistance $R_L = 0.35$. Instabilities develop on these liners, with characteristics (frequency, wavenumber, waveforms) in agreement with the linear stability analysis. For long liners, there exist several consecutive instabilities in the streamwise direction, which all have the same nature but slightly different characteristics due to the streamwise evolution of the mean flow on the liner. This was also well captured by linear stability analyses made at several streamwise stations on the liner, using the local computed mean flow. Well sustained oscillations have been observed, and this was not expected for a convectively unstable situation. It seems that at least for short enough liners as considered here, the acoustic wave travelling in the upstream direction creates a feedback loop and thus a global mode on the liner. The unstable liner also emits sound at the frequency of the instability in the downstream direction. It is the scattering of the instability at the trailing edge of the liner that generates both the upstream-propagating wave and the downstream acoustic wave. Thus, the sound wave does not seem to increase in amplitude on the liner along with the instability as the latter grows, at least in the present configuration.

The effect of an incident acoustic wave at the frequency of the instability has been studied in one configuration. It promotes the instability in the sense that it moves upstream the point at which the instability gains large amplitude, but it does not increase its amplitude in a very important way, and consequently, does not increase the level of the acoustic wave emitted downstream. If the liner were not self-oscillating in the absence of an incident wave, it is likely that the incident wave would bring more substantial changes to the system. The incident wave itself is damped by the liner, as it should, it is again the scattering of the instability at the liner trailing edge which produces sound downstream. Thus the incident acoustic wave can affect the emitted sound wave inasmuch as it modifies the instability wave on the liner.

In an on-going work, we attempt to use a global stability analysis and mode matching to model the behavior observed in the present simulations and possibly confirm the global mode of oscillation due to the backward acoustic wave. The results in this paper are based on the use of a surface impedance. That these results match existing experiments qualitatively is promessing. However, more simulations of unstable liners with impedance walls replaced by the true liner geometry are needed, and these are going to be performed in the near future. This will make it possible also to compare both types of simulations.

Acknowledgements

This work was performed using HPC resources from GENCI-CINES (Grants A0102A07582 and A0132A07582), and from the Mésocentre SPIN Calcul of the Université of Poitiers.

A Stability analysis

In this section, we give a few results on the stability analysis of the flow. The purpose is to classify the different cases as stable (R1), absolutely unstable (R023S), or convectively unstable (all other cases). The stability analysis is local since the base flow consists of the mean flow profiles at a given streamwise station x. These profiles (velocity, density, etc.) are obtained from the simulations by averaging over z and t and their remaining dependence is on y only. The equations for the stability problem are presented in [43] and applications of stability analyses on lined channel can be found in [13]. The convention is that a wave is represented by $e^{\mathrm{i}(kx-\omega t)}$, with $k = k_r + \mathrm{i}k_i$ and $\omega = \omega_r + \mathrm{i}\omega_i$. In this convention, a wave traveling toward $x > 0$ is spatially growing if $k_i < 0$. The first case considered is the one for the smallest resistance, R023S, and the flow profiles at the liner leading edge are used ($x \sim x_L \sim 35H$). First, ω is varied along contours at constant ω_i where ω_i is decreased from a large value to 0, and the unstable branches are monitored in the k-plane. The result, presented in Fig. A.1, shows that a branch initially in the upper half-plane (marked as $\mathcal{C}_1$) moves to the bottom half-plane as ω_i decrases and stays there when ω is real (marked as $\mathcal{C}_2$). This mode is then unstable. In addition the branch gets pinched by a branch coming from the bottom half-plane, forming a saddle point pattern. Therefore, this case is absolutely unstable at the leading edge of the liner. In the following, $\mathcal{C}_1$ (resp., $\mathcal{C}_2$) will be used to refer to a pre-prinching (resp., post-pinching) branch. As the flow on the liner changes with position (as observed in Fig. 10(a)) other positions should be also be checked for stability. The unstable branch at several x are shown in Fig. A.2 for $\omega \in \mathbb{R}$. At positions close to the leading edge ($35 < x < 36$) the unstable branch looks like a $\mathcal{C}_1$ branch and corresponds to absolute instability, while for downstream positions ($x \geq 36.1$) it is like a $\mathcal{C}_2$ branch, indicating that the instability is convective. The convective branch moves upward as x increases, indicating a decreasing spatial growth rate ($-k_i$) when moving away from the leading edge. Hence, case R023S has a pocket of absolute instability in the upstream part of the liner, and the instability becomes convective in the downstream part. The spatial growth rate decreases downstream. This has been generally observed for other liners as well, even if for longer liners, it can re-increase slightly downstream.

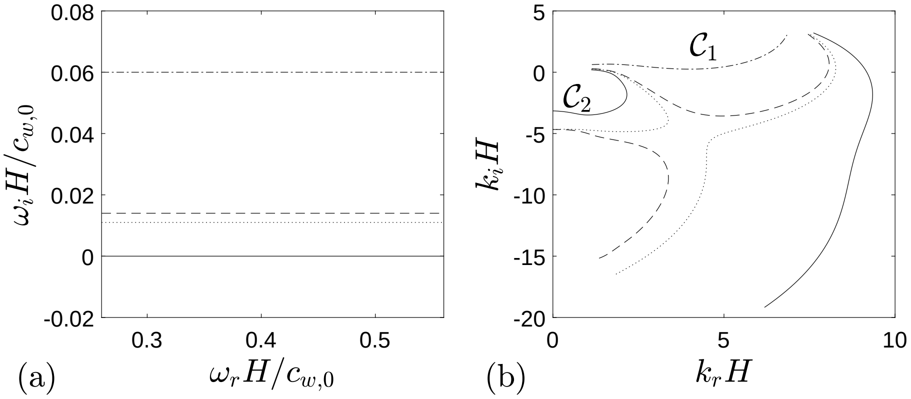

Figure A.1: Absolute instability at the liner leading edge ($x = x_L \sim 35$): (a) Some contours in the ω-plane; and (b) their mapping in the k-plane (linestyles are paired with those in (a)). Liner with $R_L = 0.23$ (case R023S).

To see what happens for other values of the liner resistance, the unstable

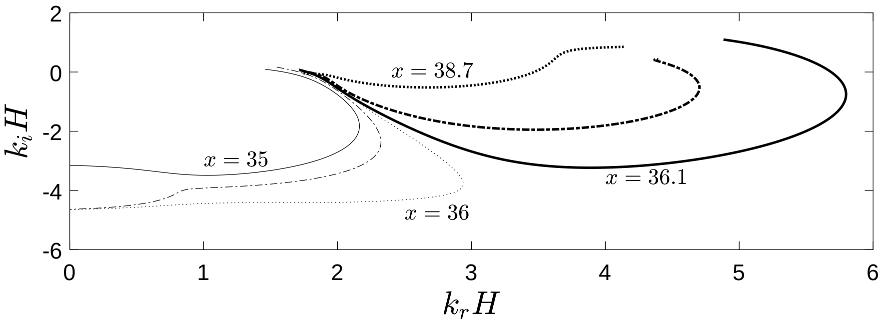

Figure A.2: Unstable branch, obtained for real ω, at several streamwise positions on the liner: —— $x = 35$ (liner leading edge); -·- $x = 35.7$; ····· $x = 36$; ▬ $x = 36.1$; -·- $x = 36.5$; ···· $x = 38.7$. Liner with $R_L = 0.23$ (case R023S).

branch is computed for $\omega \in \mathbb{R}$ and several R_L. The base flow is taken to be the one at the leading edge of the liner ($x/H \sim 35$). Figure A.3 shows that the flow is absolutely unstable for resistance smaller than $R_L = 0.29$, and convectively unstable in the range $R_L \sim 0.3 - 0.6$. For $R_L = 1$, the branch lies completely in the upper half-plane, and is therefore stable.

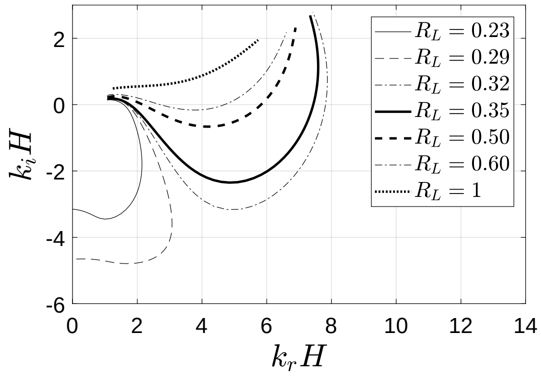

Figure A.3: Evolution of the unstable branch in the k-plane as ω is varied (with $\omega \in \mathbb{R}$), for several values of the liner resistance (R_L) and for a flow profile at the leading edge of the liner ($x/H \sim 35$).

The conclusions of this appendix are thus the following. For a liner resistance $R_L = 0.23$, the flow is absolutely unstable in the upstream part of the liner, this liner may therefore be auto-oscillating without any steady external triggering.

For $R_L = 0.35$, the liner is convectively unstable, it is not expected to oscillate in the absence of external forcing, based on a local analysis. For $R_L = 1$, the liner is stable. Except for $R_L = 0.23$, we have limited ourselves to a flow profile at the leading edge of the liner, knowing that the flow gets more stable as we move downstream on the liner. In the main text, the case $R_L = 0.35$ at other streamwise positions is investigated.

B Effect of mesh refinement

As indicated in Table 1 the mesh resolution in most of the simulations is $\Delta x^+ \sim 30$ and $\Delta z^+ \sim 10$, which is not a very fine mesh. To check the dependence of the result on the grid, the simulation R035f in Table 1 has been performed with a finer grid having $\Delta x^+ \sim 18$ and $\Delta z^+ \sim 7$. Except for the finer mesh, case R035f is the same as R035, which allows a comparison between the two simulations. The mean flow for both simulations are very close, and we first compare the mean streamwise velocity profiles in the liner region in Fig. B.1 (liner region for these cases is $35 \leq x \leq 50$). The mean velocity profiles are almost unchanged, even if one can notice a difference at positions larger than $x = 42$, and especially at $x = 44$, that is, downstream of the transition of the unstable wave. This difference is probably due to the fact that finer mesh increases the number of resolved small scales and affects the nonlinear saturation and breakdown of the instability wave, with a small effect on the mean flow.

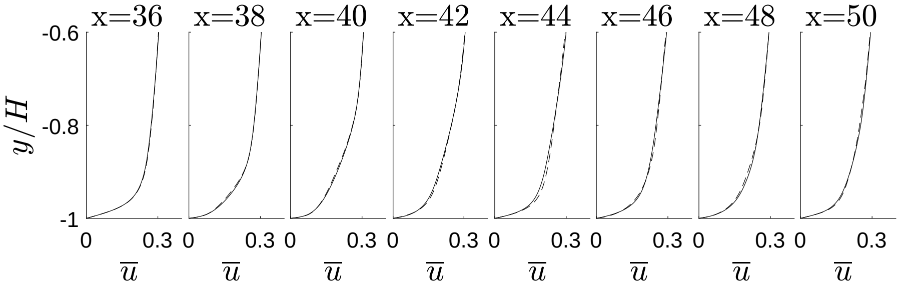

Figure B.1: Mean streamwise velocity profiles at several streamwise station above the liner (time and spanwise averaged). —— Case R035f - - - Case R035.

Concerning the unstable wave, a time-space diagram is given in Fig. B.2 for case R035f. This is very similar to the one for case R035 in Fig. 14 (of course, processes are random, an a one-to-one correspondence is not expected). However, one remarks a slightly more variable wave-pattern for case R035f, which is probably related to the slightly different nonlinear breakdown of the wave at higher spatial resolution. The computed and observed unstable wave characteristics in the linear growth regions for cases R035 and R035f were shown

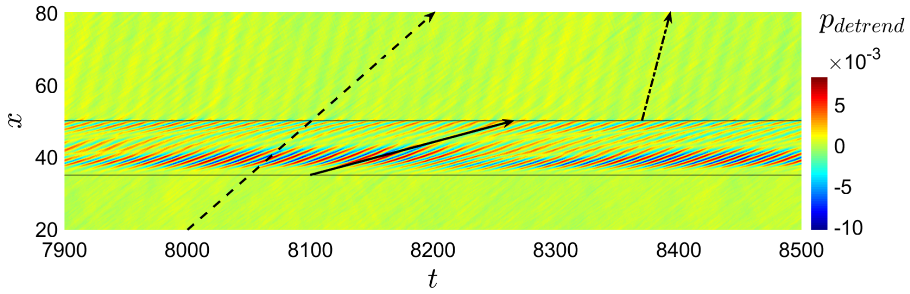

Figure B.2: Time-space diagram of (detrended) pressure at $y/H = -0.96$. For interpretation of the lines, see Fig. 14. Case R035f.

in Fig. 20. The computed characteristics depend on the local mean velocity profiles shown themselves in Fig. B.1. Figure 20 shows that the linear growth is not affected by the mesh size. Two quantities that are related to the amplitude of the unstable waves are the friction Reynolds number and the root-mean-square velocity on the liner, shown for both simulations in Fig. B.3. One observes a

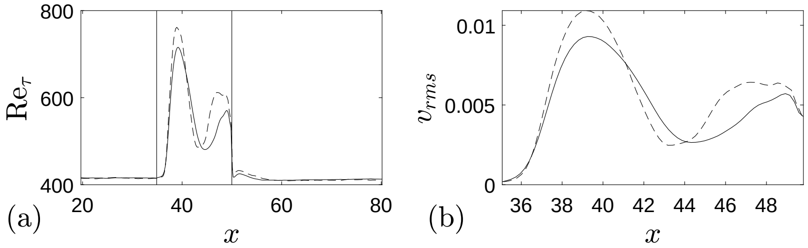

Figure B.3: (a) Friction Reynolds number on the bottom boundary; (b) root-mean-square normal velocity on the liner. —— Case R035f - - - Case R035.

qualitative agreement between the two simulations, although the amplitude of the wave is slightly dependent on the meshsize. It is not surprising in the sense that the wave is self excited. A change in the wave breakdown at $x \sim 42$ due to mesh refinement will modify the way a new wave is created in the second instability region, which will modify the feedback loop trigerring the wave in the first region. The wave amplitude at the end of the lined region at $x = 50$ is the same for both simulations, as seen in Fig. B.1(b). As a result, the sound wave downstream of the liner, produced by scattering, has the same acoustic level, as seen in Fig. B.4. Hence, except for some small quantitative differences, which are not unexpected, the two simulations performed with two different mesh resolutions provide close results.

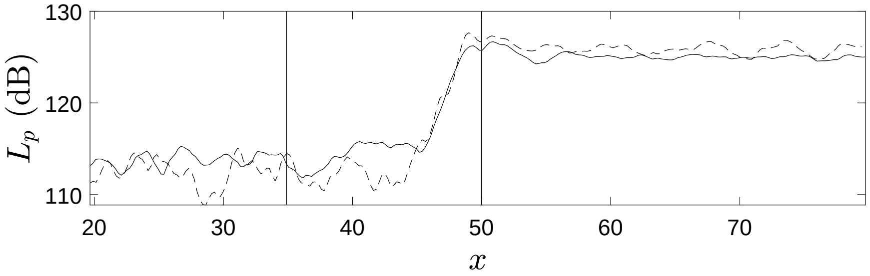

Figure B.4: Sound pressure level on the top rigid wall of the channel ($y = 1$). —— Case R035f - - - Case R035.

References

[1] A. W. Guess, Calculation of perforated plate liner parameters from specified acoustic resistance and reactance, J. Sound Vib. 40 (1975) 119–137. https://doi.org/10.1016/S0022-460X(75)80234-3.

[2] R. E. Motsinger, R. E. Kraft, Design and performance of duct acoustic treatment, in: H. H. Hubbard (Ed.) Aeroacoustics of Flight Vehicles, Acoustical Society of America, 1995, Vol. 2, pp. 165-206.

[3] M. Jones, F. Simon, R. Roncen, Broadband and Low-Frequency Acoustic Liner Investigations at NASA and ONERA, AIAA J. 60(4) (2022) pp. 2481-2500. https://doi.org/10.2514/1.J060862.

[4] J. Yang, X. Gao, W. Huang, Acoustic Experimental Technology for Aircraft Nacelle Liner. Aerospace 10, 56 (2023). doi: 10.3390/ aerospace10010056

[5] M. Brandes, D. Ronneberger, Sound Amplification in flow ducts lined with a periodic sequence of resonators, in: Proceedings of the first AIAA/CEAS aeroacoustic conference, Munich, Germany, AIAA Paper 95-126, 1995.

[6] Y. Aurégan, M. Leroux, Experimental evidence of an instability along an impedance wall with flow, J. Sound Vib. 317 (2008) 432-439. doi: 10.1016/j.jsv.2008.04.020

[7] S. Rienstra, G. Vilenski, Spatial instability of boundary layer along impedance wall, in: Proceedings of the 14th AIAA/CEAS aeroacoustic conference, Vancouver, Canada, AIAA Paper 2008-2932, 2008.

[8] D. Marx, Y. Aurégan, H. Bailliet, J.-C. Valière, PIV and LDV evidence of hydrodynamic instability over a liner in a duct with flow, J. Sound Vib. 329 (2010) 3798-3812. doi: 10.1016/j.jsv.2010.03.025

[9] S. W. Rienstra, M. Darau, Boundary-layer thickness effects on the hydrodynamic instability along an impedance wall, J. Fluid Mech. 671 (2011) 559-573. doi:10.1017/S0022112010006051

[10] E. Brambley, Acoustic implications of a thin viscous boundary layer over a compliant surface or permeable liner, J. Fluid Mech. 678 (2011) 348-378.

[11] G. Boyer, E. Piot, J.-P. Brazier, Theoretical investigation of hydrodynamic surface mode in a lined duct with sheared flow and comparison with experiments, J. Sound Vib. 330 (2011) 1793-1809. doi: 10.1016/j.jsv.2010.10.035

[12] D. Marx, A piecewise linear mean flow model for studying stability in a lined channel, J. Sound Vib. 331 (2012) 3809-3823.

[13] D. Marx, Y. Aurégan, Effect of turbulent eddy viscosity on the unstable surface mode above an acoustic liner, J. Sound Vib. 332 (2013) 3803–3820. doi: 10.1016/j.jsv.2013.02.005

[14] B. Xin, D. Sun, X. Jing, X. Sun, Numerical study of acoustic instability in a partly lined flow duct using the full linearized Navier-Stokes equations, J. Sound Vib. 373 (2016) 132–146. doi: 10.1016/j.jsv.2016.02.042

[15] D. Marx, R. Sebastian, V. Fortuné, E., Spatial Numerical Simulation of a Turbulent Plane Channel Flow with an Impedance Wall, in: Proceedings of the 25th AIAA/CEAS Aeroacoustics Conference, Deft, The Netherlands, 20-23 May 2019, AIAA Paper 2019-2543. doi: 10.2514/6.2019-2543

[16] R. Sebastian, D. Marx, V. Fortuné, Numerical simulation of a turbulent channel flow with an acoustic liner, J. Sound Vib. 456 (2019) 306-330.

[17] A. Alomar, Y. Aurégan, Particle image velocimetry measurement of an instability wave over a porous wall in a duct with flow, J. Sound Vib. 386(2017), 208–224. doi: 10.1016/j.jsv.2016.09.034

[18] S. W. Rienstra, A classification of duct modes based on surface waves, Wave motion 37 (2003) 119-135. doi: 10.1016/S0165-2125(02)00052-5

[19] E. J. Brambley, N. Peake, Classification of aeroacoustically relevant surface modes in cylindrical lined ducts, Wave motion 43 (2006) 301-310. doi: 10.1016/j.wavemoti.2006.01.001

[20] B. J. Tester, The propagation and attenuation of sound in lined ducts containing uniform or plug flow, J. Sound Vib. 28(2) (1973) 151-203. doi: 10.1016/S0022-460X(73)80102-6

[21] X. Dai, Y. Aurégan, Hydrodynamic instability and sound amplification over a perforated plate backed by a cavity, in: Proceedings of the 25th AIAA/CEAS Aeroacoustics Conference, Deft, The Netherlands, 20-23 May 2019, AIAA Paper 2019-2703. doi : 10.2514/6.2019-2703

[22] E. J. Brambley, M. Darau, S. W. Rienstra, The critical layer in linear-shear boundary layers over acoustic linings, J. Fluid Mech. 710 (2012) 545-568. doi: 10.1017/jfm.2012.376

[23] M. J. King, E. J. Brambley, R. Liupekevicius, M. Radia, P. Lafourcade, T. H. Shah, The critical layer in quadratic flow boundary layers over acoustic linings, J. Fluid Mech. 950 (2022) A8. doi: 10.1017/jfm.2022.753

[24] E. J. Brambley, Fundamental problems with the model of uniform flow over acoustic linings, J. Sound Vib. 322 (2009) 1026-1037. doi:10.1016/j.jsv.2008.11.021

[25] E. J. Brambley, Well-posed boundary condition for acoustic liners in straight ducts with flow, AIAA J. 49 (2011) 1272-1282. doi:10.2514/1.J050723

[26] C. K. W. Tam, L. Auriault, Time-Domain Impedance Boundary Conditions for Computational Aeroacoustics, AIAA J. 34(5) (1996) 917-923. doi: 10.2514/3.13168

[27] Y. Ozyoruk, L. N. Long, Time-domain calculation of sound propagation in lined ducts with sheared flows, AIAA J. 39(5) (2000) 768–773. doi: 10.2514/2.1056

[28] K. Y. Fung, H. Ju, Broadband time-domain impedance models, AIAA J. 39 (2001) 1449–1454.

[29] Y. Reymen, M. Baelmans, W. Desmet, Efficient implementation of Tam and Auriault's time-domain impedance boundary condition, AIAA J. 46 (2008) 2368–2376. doi: 10.2514/1.35876

[30] G. Gabard, E. Brambley, A full discrete dispersion analysis of time-domain simulations of acoustic liners with flow, J. Comput. Phys. 273 (2014) 310–326. doi: 10.1016/j.jcp.2014.05.004

[31] D. Marx, Numerical Computation of a lined duct instability using the linearized Euler equations, AIAA J. 53 (8) (2015) 2379-2388.

[32] Y. Deng, A. Alomar , D. Dragna , M.-A. Galland, Characterization and suppression of the hydrodynamic instability in the time domain for acoustic propagation in a lined flow duct, J. Sound Vib. 500 (2021) 115999. doi: 10.1016/j.jsv.2021.115999

[33] J. Jimenez, M. Uhlmann, A. Pinelli, G. Kawahara, Turbulent shear flow over active and passive porous surfaces, J. Fluid Mech. 442 (2001) 89-117.

[34] C. Scalo, J. Bodart, S. Lele, Compressible turbulent channel flow with impedance boundary conditions, Phys. Fluids 27 (2015) 035107.

[35] C. K. W. Tam, H. Ju, B. E. Walker, Numerical Simulation of a Slit Resonator in a Grazing Flow Under Acoustic Excitation, J. Sound Vib. 313 (2008) 449–471.

[36] Q. Zhang, D. J. Bodony, Numerical investigation and modelling of acoustically excited flow through a circular orifice backed by a hexagonal cavity, J. Fluid Mech. 693 (2012) 367–401.

[37] Q. Zhang, D. J. Bodony, Numerical investigation of a honeycomb liner grazed by laminar and turbulent boundary layers, J. Fluid Mech. 792 (2016) 936–980. doi: 10.1017/jfm.2016.79

[38] L. M. Pereira, L. A. Bonomo, A. R. da Silva, J. Cordioli, Lattice-Boltzmann Numerical Investigation of a Realistic Multi-Cavity Acoustic Liner with Grazing Flow, in: Proceedings of the 28th AIAA/CEAS Aeroacoustics Conference, Southampton, UK, 14-17 June 2022, AIAA Paper 2022-2967. doi: 10.2514/6.2022-2967

[39] C. K. W. Tam, N. N. Pastouchenko, M. G. Jones, W. R. Watson, Experimental validation of numerical simulations for an acoustic liner in grazing flow: Self-noise and added drag, J. Sound Vib. 333 (2014) 2831–2854. doi: 10.1016/j.jsv.2014.02.019

[40] D. Marx, Numerical simulation of physical instabilities in a lined channel using the linearized Euler Equations, in: Proceedings of the 14ème Congrès d'Acoustique, Poitiers, France, 22-25 april 2014.

[41] D. K. Singh, S. W. Rienstra, Nonlinear asymptotic impedance model for a Helmholtz resonator liner, J. Sound Vib. 333 (2014) 3536–3549. doi: 10.1016/j.jsv.2014.03.013

[42] F. Monteghetti, D. Matignon, E. Piot, Energy analysis and discretization of nonlinear impedance boundary conditions for the time-domain linearized Euler equations, J. Comput. Phys. 375 (2018) 393–426. doi: 10.1016/j.jcp.2018.08.037

[43] D. Marx, Developed spatial turbulent channel flow simulation for acoustic wave propagation, Comput. Fluids 245 (2022) 105586. doi: 10.1016/j.compfluid.2022.105586

[44] T. Poinsot, S. K. Lele, Boundary conditions for direct simulations of compressible viscous flows, J. Comput. Phys. 101 (1992) 104–129.

[45] C. S. Yoo, Y. Wang, A. Trouvé, H. G. Im, Characteristic boundary conditions for direct simulations of turbulent counterflow flames, Combustion Theory and Modelling 9 (2005) 617–646.

[46] G. Daviller, G. Oztarlik, T. Poinsot, A generalized non-reflecting inlet boundary condition for steady and forced compressible flows with injection of vortical and acoustic waves, Comput. Fluids 190 (2019) 503–513.

[47] W. Polifke, C. Wall, P. Moin, Partially reflecting and non-reflecting boundary conditions for simulation of compressible viscous flow, J. Comput. Phys 213 (2006) 437–449.

[48] L. Selle, F. Nicoud, T. Poinsot, Actual impedance of nonreflecting boundary conditions: implications for computation of resonators, AIAA J. 42 (2004) 958–964.

[49] B. Gustafsson, H.-O. Kreiss, J. Oliger, Time dependent problems and difference methods, John Wiley & Sons, New York Inc., 1995.

[50] A. E. Honein, P. Moin, Higher entropy conservation and numerical stability of compressible turbulence simulations, J. Comput. Phys. 201 (2004) 531–545.

[51] S. K. Lele, Compact finite difference schemes with spectral-like resolution, J. Comput. Phys. 103 (1992) 16–42.

[52] F. Kremer, C. Bogey, C. Bailly, Semi-implicit Runge-Kutta Schemes: development and application to compressible channel flow, AIAA J. 52 (2014) 516–527.

[53] Y. Kametani, K. Fukagata, R. Orlu, P. Schlatter, Effect of uniform blowing/suction in a turbulent boundary layer at moderate Reynolds number, Int. J. Heat Fluid Flow 55 (2015) 132–142. doi: 10.1016/j.ijheatfluidflow.2015.05.019

[54] R. D. Moser, J. Kim, N. N. Mansour, Direct numerical simulation of turbulent channel flow up to Re_τ= 590, Phys. Fluids 11(4) (1999) 943–945.

[55] M. Abom, Modal decomposition in ducts based on transfer function measurements between microphone pairs, J. Sound Vib. 135 (1989) 95–114.

[56] A. Almunif, L. Fan, Z. Miao, A tutorial on data-driven eigenvalues identification: Prony analysis, matrix pencil, and eigensystem realization algorithm, Int. Trans. Electr. Energ. Syst. (2020) e12283. doi: 10.1002/2050-7038.12283

[57] W. R. Watson, M. H. Carpenter, M. G. Jones, Performance of Kumaresan and Tufts algorithm in liner impedance eduction with flow, AIAA J. 53 (2015) 1091–1102. doi: 10.2514/1.J053705

[58] T. K. Sarkar, O. Pereira, Using the matrix pencil method to estimate the parameters of a sum of complex exponentials, IEEE Antennas Propag. Mag. 37 (1995) 48–55.

[59] M. Gavish, D. L. Donoho, The optimal hard threshold for singular values is $4/\sqrt{3}$, IEEE Trans. Inf. Theory 60 (2014) 5040–5063.

[60] D. J. Trudnowski, J. M. Johnson, J. F. Hauer, Making Prony analysis more accurate using multiple signals, IEEE Trans. Power Syst., 14 (1999) 226–231. doi: 10.1109/59.744537.

[61] S. K. Robinson, Coherent motions in the turbulent boundary layer, Annu. Rev. Fluid Mech 23 (1991) 601–639. doi: 10.1146/annurev.fl.23.010191.003125

[62] C. Liu, L. Chen, Parallel DNS for vortex structure of late stages of flow transition, Comput. Fluids 45 (2011) 129–137. doi: 10.1016/j.compfluid.2010.11.006

[63] L. Pascal, E. Piot, G. Casalis, Global linear stability analysis of flow in a lined duct, J. Sound Vib. 410 (2017) 19–34. doi: 10.1016/j.jsv.2017.08.007

[64] J. S. Bendat, A. G. Piersol, Random Data - Analysis and measurement procedures, second ed., John Wiley & Sons, New York, 1986.